universe

MDPI

*Article*

# Centrality Evolution of Transverse Momentum Spectra of Identified Light-Flavor Hadrons in $p$+Pb Collisions at $\sqrt{s_{nn}}$ = 5.02 TeV at the LHC Within a Two-Component Model

**Khusniddin K. Olimov [1,2,*], Anastasiya Fedosimova [3,4], Fu-Hu Liu [5,*], Kobil A. Musaev [1], Igor A. Lebedev [3], Shokhida A. Khudoyberdieva [1], Azizjon Tokhirov [1], Sayora Ibraimova [3] and Ekaterina Bondar [3]**

1 Physical-Technical Institute of Uzbekistan Academy of Sciences, Chingiz Aytmatov Str. 2b, Tashkent 100084, Uzbekistan; qobilmusayev1986@gmail.com (K.A.M.); xudoyberdiyevashohida676@gmail.com (S.A.K.); atohirov54@gmail.com (A.T.)
2 Department of Natural Sciences, National University of Science and Technology MISIS (NUST MISIS), Almalyk Branch, Almalyk 110100, Uzbekistan
3 Institute of Physics and Technology, Satbayev University, Almaty 050032, Kazakhstan; ananastasia@list.ru (A.F.); lebedev@sci.kz (I.A.L.); sayara_ibraimova@mail.ru (S.I.); bondar@sci.kz (E.B.)
4 Institute of Nuclear Physics, Almaty 050032, Kazakhstan
5 Institute of Theoretical Physics, Shanxi University, Taiyuan 030006, China
* Correspondence: khkolimov@gmail.com (K.K.O.); fuhuliu@sxu.edu.cn (F.-H.L.)

**Abstract**

Using the two-component Tsallis-Hagedorn Model with Transverse Flow (THMTF), this study analyzes centrality dependencies of midrapidity transverse momentum ($p_T$) spectra for identified light-flavor hadrons in asymmetric $p$+Pb collisions at $\sqrt{s_{nn}}$ = 5.02 TeV, comparing them with symmetric Pb+Pb collision data at $\sqrt{s_{nn}}$ = 2.76 and 5.02 TeV at the LHC. The analysis successfully describes ALICE experimental data up to $p_T$ = 20 GeV/$c$ across seven multiplicity classes in $p$+Pb collisions, estimating that collective flow emerges at $\langle N_{part} \rangle \approx 4.0 \pm 0.5$ along with simultaneous transitioning of kinetic freeze-out temperature to a nearly plateau region. The kinetic freeze-out temperature parameter shows distinct, system-dependent behavior before stabilization with an increase in $\langle N_{part} \rangle$ in $p$+Pb and Pb+Pb collisions at the LHC. Furthermore, the findings suggest that collective flow and particle production correlate with increased thermalization, with spectral analysis indicating different dynamics at hard $p_T$ region between p+Pb and Pb+Pb collision systems.

**Keywords:** high-energy $p$+Pb and Pb+Pb collisions at the LHC; transverse momentum spectra of identified light-flavor hadrons; QCD-inspired Hagedorn function; Tsallis distribution with embedded transverse flow; two-component model function; power-index $n$; momentum scale parameter $P_0$; non-extensivity parameter $q$; transverse flow velocity; kinetic freeze-out temperature; mechanisms of hadron production at the LHC; (crossover) phase transition from the dense hadronic matter to QGP state; correlations among kinetic freeze-out parameters

Check for updates

Academic Editors: Jun Xu and Chunjian Zhang

Received: 20 July 2026
Revised: 20 August 2026
Accepted: 26 August 2026
Published: 28 August 2026

**Copyright:** © 2026 by the authors. Licensee MDPI, Basel, Switzerland. This article is an open access article distributed under the terms and conditions of the Creative Commons Attribution (CC BY) license.

## 1. Introduction

High-energy Xe+Xe and Pb+Pb collisions at the LHC (Large Hadron Collider, Switzerland) are primarily aimed at producing QGP (Quark-Gluon Plasma), a very dense state of nearly free quarks and gluons, and studying its various properties and evolution along

with understanding the strong interaction at extreme matter densities. Our Universe is believed to have been in a QGP state a few microseconds after the Big Bang, which marks the origin of the Universe. Production of QGP was firmly established [1–9] in high-energy Au+Au and Pb+Pb collisions at the RHIC (Relativistic Heavy-Ion Collider, Brookhaven National Laboratory, New York, USA) and LHC/CERN experiments. QGP with a very short lifetime of the order of $10^{-23}$ s behaves as nearly perfect quark-gluon liquid with very small viscosity [8,9]. Produced QGP decays very quickly into a large number of particles during the hadronization stage. Afterwards, a very dense and hot system of produced hadrons, called fireball, expands and cools down very swiftly, going through the chemical and kinetic freeze-out stages. At the chemical freeze-out, the particles of a fireball stop interacting inelastically, which fixes the numbers of produced hadron species. The temperature of the system ($T_{\rm ch}$) and chemical potential ($\mu$) at the chemical freeze-out stage are extracted from yield ratios of various particle species using thermal or statistical hadronization models [10–15]. At the kinetic freeze-out, the particles of the fireball stop interacting elastically, and the momenta and energies of the final particles do not change anymore until they reach detectors. Therefore, it is important to analyze the transverse momentum ($p_T$) distributions of the final particles with the help of various thermodynamic and phenomenological models to extract the thermodynamic and hydrodynamic parameters of the fireball at the moment of kinetic freeze-out.

Traditionally, analysis of high-energy proton-proton and proton-nucleus collisions was considered as a reference study to extract the collective parameters of the collision system, including those of QGP, in high-energy nucleus-nucleus collisions at the same center-of-mass collision energy per nucleon pair. However, many signatures of QGP production, like significant enhancement of yield of multi-strange particles with respect to non-strange hadrons and development of a strong radial flow, were also observed [16–45] in high-energy proton-proton and proton-nucleus collisions. The proton-to-pion yield ratio did not change with multiplicity, while the ratios of a strange-hadron to pion yields increased considerably with an increase in multiplicity in proton-proton collisions at $\sqrt{s}$ = 7 TeV at midrapidity at the LHC [19]. Larger enhancement was observed for hadrons with a higher strangeness content [19]. The thermal abundances in the hadron yields in high-energy proton-proton collisions, along with an exponential component found in their $p_T$ spectra, were considered as the clear signature of thermalization [27,31]. Measurements revealed [41,42] strong azimuthal, long-range particle correlations (the "ridge" effect) in $p$+Pb collisions at $\sqrt{s_{nn}}$ = 5.02 TeV at the LHC. The development of a significant collective radial flow in high-energy proton-proton collisions with large enough multiplicities was demonstrated in Refs. [20,24,25,33,34]. Strong flow-like effects were also reported [39–43] in high-multiplicity $p$+Pb collisions at $\sqrt{s_{nn}}$ = 5.02 TeV at the LHC. The evidence of significant radial flow developed with increasing centrality of $p$+Pb collisions at the LHC was given in Refs. [44,45]. Investigation of various properties of proton-lead ($p$+Pb) collisions at the LHC is especially important because it bridges the gap between elementary proton-proton collisions and heavy-ion (Pb+Pb) collisions.

The present work is an important extension of our recent work [45], which was devoted to the analysis of the evolution of the kinetic freeze-out parameters in $p$+Pb collisions at $\sqrt{s_{nn}}$ = 5.02 TeV at the LHC with changing collision centrality, expressed by $\langle N_{part} \rangle$. The analysis of Ref. [45] was performed via simultaneous minimum $\chi^2$ fits in the $p_T$ region up to 5 GeV/$c$ of the midrapidity $p_T$ spectra of the charged pions and kaons, protons and antiprotons, measured by the ALICE Collaboration [43], using a Tsallis distribution function with embedded transverse flow. In Ref. [43] the $\langle N_{part} \rangle$ dependencies of the global transverse flow velocity parameter, $\langle \beta_T \rangle$, common kinetic freeze-out temperature, $T_0$, and non-extensivity parameter, $q$, for particle species of Tsallis function with incorporated

transverse flow in $p$+Pb collisions at $\sqrt{s_{nn}}$ = 5.02 TeV were analyzed. The transverse flow velocity ($\langle\beta_T\rangle$) was absent at the first $\langle N_{part}\rangle$ point, corresponding to 80–100% centrality of $p$+Pb collisions, and then $\langle\beta_T\rangle$ started emerging and increased further with an increase in $\langle N_{part}\rangle$. The border (threshold) $\langle N_{part}\rangle$ value, where the collective transverse flow starts emerging simultaneously with $T_0$ transitioning to almost constant (plateau) region in $p$+Pb collisions at $\sqrt{s_{nn}}$ = 5.02 TeV, was estimated to be $\langle N_{part}\rangle \approx 4.0 \pm 0.5$. Non-extensivity parameter $q$ decreased systematically for all studied particle species with an increase in $\langle N_{part}\rangle$, suggesting an increase in degree of the system thermalization and equilibrium with centrality of $p$+Pb collisions at $\sqrt{s_{nn}}$ = 5.02 TeV, in agreement with the similar result obtained in high-energy Xe+Xe and Pb+Pb collisions at the LHC [46–48]. Inequality $q$ (kaons) > $q$ (pions) > $q$ ((anti)protons) was observed for non-extensivity parameter $q$ in $p$+Pb collisions at $\sqrt{s_{nn}}$ = 5.02 TeV, in agreement with the relation $q$(baryons) < $q$(mesons), established previously [33,34,46–48] in high-energy proton-proton and nucleus-nucleus collisions.

Transverse momentum distributions of particles generated in high-energy collisions are characterized by exponential behavior in the low-$p_T$ part and power-like distribution, typical for perturbative Quantum-Chromo-Dynamics (pQCD), in the high-$p_T$ part. The low-$p_T$ part ($p_T$ < 2 GeV/$c$) of hadron spectra contains valuable information about the collective radial expansion and thermal parameters of the system at kinetic freeze-out along with resonance decays [9]. Quark recombination processes, which lead to an enhancement of the proton-to-pion yield ratio in nuclear collisions compared to proton-proton collisions, contribute mainly to the intermediate $p_T$ range (2 GeV/$c$ < $p_T$ < 4–5 GeV/$c$) of transverse momentum spectra. Quark and gluon fragmentation, QCD hard scatterings, production of quark-gluon jets and their energy loss in the QGP medium, contribute mostly to the hard-$p_T$ part ($p_T$ > 5 GeV/$c$) of hadron spectra [9]. While hard-$p_T$ hadrons originate mostly from parton (quark or gluon) fragmentation, the dense QGP matter formed in nuclear collisions allows for partons to recombine, which favors baryon over meson production mainly in the intermediate $p_T$ range [9]. There are no exact $p_T$ borders between various processes and mechanisms, contributing to the measured $p_T$ spectra of hadrons and overlapping significantly in different $p_T$ regions. Unfortunately, these various processes and mechanisms, contributing differently to the final $p_T$ spectra of hadrons, still lack an unambiguous theoretical description and can be reproduced by various phenomenological models only.

Here it is worth commenting on the pioneering work of Bediaga et al. [49], who successfully applied Tsallis nonextensive statistics to model hadron production in high-energy $e^+$+$e^-$ collisions, showing that a nonextensive entropic index of $q \approx 1.1$ accurately fits high-energy experimental data. This work demonstrated [49] that high-energy collisions create systems with long-range correlations, requiring a modified thermodynamic equilibrium to explain power-law tails in transverse momentum distributions. This study [49] is one of the foundational works for using nonextensive statistics in high-energy physics to facilitate analysis of complex collisions at the LHC and RHIC.

To reproduce accurately the measured long $p_T$ ranges of the midrapidity $p_T$ distributions of charged particles at various centralities of high-energy heavy-ion collisions at the LHC, the specific two-component model function, which is the sum of thermodynamically consistent Tsallis function with embedded transverse flow and inverse power-law function (which is asymptotic of QCD-inspired Hagedorn function at high $p_T$ values), was proposed in our recent work [50]. The first and second terms of this two-component model function are assumed to describe the soft (low) and hard components, respectively, of midrapidity transverse momentum distributions of hadrons in high-energy collisions. This new two-component model function, called Tsallis-Hagedorn model with transverse flow (THMTF), described [50] very well the experimental midrapidity transverse momentum spectra of primary charged particles in the whole $p_T$ range up to 50 GeV/$c$, measured by ALICE

Collaboration in minimum bias p+p collisions at $\sqrt{s}$ = 2.76 and 5.02 TeV [51], minimum bias $p$+Pb collisions at $\sqrt{s_{nn}}$ = 5.02 TeV [51], and nine collision centrality intervals of Xe+Xe collisions at $\sqrt{s_{nn}}$ = 5.44 TeV [52] and Pb+Pb collisions at $\sqrt{s_{nn}}$ = 2.76 and 5.02 TeV [51]. The dependencies of the extracted parameters of THMTF function on Xe+Xe and Pb+Pb collision centrality at the LHC, expressed by $\langle N_{part} \rangle$ as well as $\langle dN_{ch}/d\eta \rangle$, and c.m. collision energy (per nucleon pair) were analyzed and interpreted successfully in Ref. [50].

The main aim of the present work is to analyze the centrality ($\langle N_{part} \rangle$) dependencies of midrapidity $p_T$ spectra of the charged pions and kaons, protons and antiprotons in the whole measured $p_T$ range at seven centrality classes, expressed by $\langle N_{part} \rangle$, in $p$+Pb collisions at $\sqrt{s_{nn}}$ = 5.02 TeV at the LHC, measured [43] by the ALICE collaboration, using the new two-component THMTF model function, introduced and probed successfully in Ref. [50]. The trends of $\langle N_{part} \rangle$ dependencies of the parameters of the two-component THMTF model function, obtained in the present work in $p$+Pb collisions at $\sqrt{s_{nn}}$ = 5.02 TeV at the LHC, will be compared systematically with the $\langle N_{part} \rangle$ tendencies of the corresponding parameters of the same model function, established recently [50] in Pb+Pb collisions at $\sqrt{s_{nn}}$ = 2.76 and 5.02 TeV at the LHC.

## 2. The Experimental Data and Two-Component Model

In the present work, we analyze the midrapidity ($|y| < 0.5$) transverse momentum distributions of the charged pions and kaons, protons and antiprotons measured [43] at seven centrality intervals in $p$+Pb collisions at $\sqrt{s_{nn}}$ = 5.02 TeV by the ALICE Collaboration. The average numbers of participant nucleons ($\langle N_{part} \rangle$) and $\langle dN_{ch}/d\eta \rangle$ values, calculated in Refs. [53,54], respectively, in seven centrality classes of $p$+Pb collisions at $\sqrt{s_{nn}}$ = 5.02 TeV, are shown in Table 1.

**Table 1.** The calculated average number of participant nucleons [53] and $\langle dN_{ch}/d\eta \rangle$ [54] in the analyzed centrality classes of $p$+Pb collisions at $\sqrt{s_{nn}}$ = 5.02 TeV. The mean values and their uncertainties are obtained by the ALICE Collaboration with Glauber Monte Carlo Calculations.

| Centrality | $\langle N_{part} \rangle$ | $\langle dN_{ch}/d\eta \rangle$ |
|---|---|---|
| 0–5% | 15.10 ± 0.75 | 41.4 ± 1.5 |
| 5–10% | 13.5 ± 0.7 | 35.1 ± 1.3 |
| 10–20% | 12.2 ± 0.6 | 31.0 ± 1.1 |
| 20–40% | 10.1 ± 0.5 | 24.5 ± 0.9 |
| 40–60% | 7.4 ± 0.3 | 17.1 ± 0.6 |
| 60–80% | 4.9 ± 0.1 | 10.8 ± 0.4 |
| 80–100% | 2.99 ± 0.03 | 4.8 ± 0.2 |

The following equation [55–57] of non-extensive Tsallis distribution [58–60] function, derived for a zero chemical potential ($\mu \approx 0$ at the TeV energy range) at midrapidity ($<y> = 0$), satisfies the thermodynamic relations for pressure, temperature, particle number, energy, and entropy densities [56]:

$$\frac{d^2N}{2\pi N_{ev} p_T dp_T dy} = C_q \cdot m_T \cdot \left(1 + (q-1) \cdot \frac{m_T}{T}\right)^{-q/(q-1)}, \quad (1)$$

where $C_q$ is the fitting constant, $N_{ev}$—the total number of inelastic collision events, $m_T = \sqrt{p_T^2 + m_0^2}$—the transverse energy (mass), and $m_0$ is the hadron's rest mass. Parameter $T$ is the effective temperature, and $q$ is the non-extensivity parameter. The parameter $q$ is fundamental for the Tsallis distribution, and it describes the fluctuations in

the system's temperature through the relationship $q - 1 = \frac{Var(T)}{<T>^2}$. The difference from unity of this parameter, $q - 1$, is assumed to quantify the degree of non-thermalization and non-equilibrium within the system. When $q$ approaches 1, the Tsallis distribution transitions to the exponential Boltzmann-Gibbs distribution, which describes systems in equilibrium. The closer the $q$ parameter is to one (1), the larger the degree of thermalization (equilibrium) of the system. We call the function in Equation (1) the thermodynamically consistent Tsallis function. The thermodynamic consistency of the function in Equation (1) was proved in Ref. [56]. The normalization constant is related to the system's freeze-out volume (V) [55,56] via the expression $C_q = gV/(2\pi)^3$, where $g$ is the degeneracy factor of the hadron species.

The effective temperature ($T$) in Equation (1) comprises contributions from both chaotic thermal motion and transverse radial flow. To separate these two factors, the velocity of transverse flow should be incorporated into the Tsallis distribution function. The transverse flow is incorporated into a thermodynamically consistent Tsallis distribution in Equation (1) by substitution $m_{\mathrm{T}} \to \langle\gamma_{\mathrm{T}}\rangle(m_{\mathrm{T}} - p_{\mathrm{T}}\langle\beta_{\mathrm{T}}\rangle)$, as made for the first time in Ref. [46], to obtain the function:

$$\frac{d^2N}{2\pi N_{ev} p_{\mathrm{T}} dp_{\mathrm{T}} dy} = C_q \cdot \langle\gamma_{\mathrm{T}}\rangle \cdot (m_{\mathrm{T}} - p_{\mathrm{T}} \cdot \langle\beta_{\mathrm{T}}\rangle) \left(1 + \langle\gamma_{\mathrm{T}}\rangle \cdot \frac{(q-1)\cdot(m_{\mathrm{T}} - p_{\mathrm{T}}\cdot\langle\beta_{\mathrm{T}}\rangle)}{T_0}\right)^{-q/(q-1)}, \quad (2)$$

The substitution $m_T \to \langle\gamma_T\rangle(m_T - p_T\langle\beta_T\rangle)$ means [46] the Lorentz transformation to a system co-moving with an average transverse flow velocity, $\langle\beta_T\rangle$, of the system of particles in the transverse plane, assuming that such a flow of particles exists in this system. The thermodynamically consistent Tsallis function with embedded transverse flow in Equation (2) reproduced [45–48] very well the midrapidity $p_{\mathrm{T}}$ spectra of identified charged hadrons in the low and intermediate $p_{\mathrm{T}}$ ranges up to 5 GeV/$c$ in high-energy $p$+Pb, Xe+Xe, and Pb+Pb collisions at the LHC, allowing for the physically meaningful interpretation of the obtained freeze-out parameters and their dependencies on collision centrality ($\langle N_{part}\rangle$) and system size.

The following inverse power law—QCD-inspired Hagedorn function [61–63] reproduced very well the high transverse momentum part of $p_{\mathrm{T}}$ spectra of hadrons in nucleon-nucleon collisions at high energies:

$$\frac{d^2N}{2\pi N_{ev} p_{\mathrm{T}} dp_{\mathrm{T}} dy} = C_n \cdot \left(1 + \frac{p_T}{P_0}\right)^{-n}, \quad (3)$$

where $C_n$ is the fitting constant, proportional to the freeze-out volume of the system, and $n$ and $P_0$ are free parameters, which are related to underlying mechanisms of hadron production. Parameter $P_0$ is the characteristic momentum scale, and it represents the typical momentum scale where the production mechanism transitions from soft (thermal/exponential) to hard (power-law/perturbative) processes. This parameter could also feature the average transverse momentum, contributed by partons before they fragment into hadrons. The power-index parameter $n$ characterizes the hardness of the interaction. A low value of $n$ reflects a hard spectrum dominated by perturbative QCD (pQCD) scattering and jet production. The QCD cross sections at high energies are demonstrated [61,64] to scale as $\cdot(p_T)^{-n}$, in which the power-index $n$ can be phenomenologically expressed as $n = 2\cdot n_\alpha - 4$, where $n_\alpha$ is the number of active flavors or the number of partons (quarks or gluons) participating in a scattering. For the leading twist, simple scattering, the dominant process is a simple point-like scattering between two quarks, $q + q \to q + q$, with the number of participating partons, $n_\alpha$ = 4. This leads to the power-index parameter $n = 2\cdot n_\alpha - 4 = 4$. For the higher twist, multiple scattering, multiple quark-quark or quark-hadron scatterings occur, resulting in an increase in the $n$ value. This shows involvement of

more constituent participants in particle production. The $n$ value varies significantly as a function of the constituent quark content, differing between mesons and baryons. These variations in the $n$-value stem from the distinct quark structures and production mechanisms of mesons and baryons, explicitly depending on the number of constituent partons required to coalesce into the final hadron. Within a statistical framework, the Hagedorn parameter $n$ scales inversely with the Tsallis non-extensivity parameter $q$ according to the relation $n = 1/(q-1)$.

In the limit of high $p_{\mathrm{T}}$, the QCD-inspired Hagedorn function in Equation (3) reduces to the asymptotic form of a simple inverse power law:

$$\frac{d^2N}{2\pi N_{ev} p_{\mathrm{T}} dp_{\mathrm{T}} dy} = C_n \cdot \left(\frac{p_T}{P_0}\right)^{-n}. \tag{4}$$

In order to accurately describe the measured long $p_{\mathrm{T}}$ ranges of midrapidity transverse momentum spectra for charged particles at different centralities in high-energy heavy-ion and proton–proton collisions, a new two-component model function composed of the sum of a thermodynamically consistent Tsallis function with embedded transverse flow (Equation (2)) and a simple inverse power-law function (Equation (4)) was proposed recently in our work [50]:

$$\frac{d^2N}{2\pi N_{ev} p_{\mathrm{T}} dp_{\mathrm{T}} dy} = \\ = \theta(x_{thr} - p_T) \cdot C_q \cdot \langle \gamma_{\mathrm{T}} \rangle \cdot (m_{\mathrm{T}} - p_{\mathrm{T}} \cdot \langle \beta_{\mathrm{T}} \rangle) \cdot \left(1 + \langle \gamma_{\mathrm{T}} \rangle \cdot \frac{(q-1) \cdot (m_{\mathrm{T}} - p_{\mathrm{T}} \cdot \langle \beta_{\mathrm{T}} \rangle)}{T_0}\right)^{-q/(q-1)} + \theta(p_T - x_{thr}) \cdot C_n \cdot \left(\frac{p_T}{P_0}\right)^{-n}, \tag{5}$$

where $\theta(x)$ is the Heaviside function with the following properties: $\theta(x) = 0$ if $x < 0$, and $\theta(x) = 1$ if $x > 0$. This two-component model function in Equation (5) is called the Tsallis-Hagedorn model with transverse flow (THMTF). Parameter $x_{thr}$ is the optimal value of $p_{\mathrm{T}}$ border between the corresponding $p_{\mathrm{T}}$ fit ranges of the first and second term in Equation (5). The first term in Equation (5) is assumed to describe the low (soft) and intermediate $p_{\mathrm{T}}$ range, while the second term should describe the high (hard) $p_{\mathrm{T}}$ region. It is well known that at the TeV collision energy range at the LHC, soft bulk particle production dominates below $p_{\mathrm{T}} \approx 2$ GeV/$c$, while above $p_{\mathrm{T}} \approx 4$–$5$ GeV/$c$ hard fragmentation becomes the primary mechanism for particle production. In our work, we use fixed $x_{thr} = 5$ GeV/$c$ to make sure that $p_{\mathrm{T}} > 5$ GeV/$c$ region is practically entirely governed by the hard scattering perturbative QCD processes, described by the second power-law term in Equation (5). Moreover, the first term in Equation (5), expressed by a thermodynamically consistent Tsallis function with incorporated transverse flow, given in Equation (2), reproduced very well the midrapidity transverse momentum distributions of identified charged particles at various centralities of high-energy heavy-ion collisions in the low and intermediate $p_{\mathrm{T}}$ range up to $p_{\mathrm{T}} = 5$ GeV/$c$ [45–48]. Using $x_{thr} = 5$ GeV/$c$ in Equation (5) denotes that the hadron $p_{\mathrm{T}}$ spectrum is reproduced by a thermodynamically consistent Tsallis function with embedded transverse flow (Equation (2)) in $p_{\mathrm{T}} \leq 5$ GeV/$c$ region and by an inverse power-law function (Equation (4)) in $p_{\mathrm{T}} > 5$ GeV/$c$ range.

To study the correlation between two sets of parameters $x$ and $y$ of the two-component model function in Equation (5) in the present work, we calculate the Pearson coefficient of linear correlation as follows:

$$R(x,y) = \frac{\sum_{i=1}^{n} (x_i - < x >) \cdot (y_i - < y >)}{\sqrt{\sum_{i=1}^{n} (x_i - < x >)^2 \cdot \sum_{i=1}^{n} (y_i - < y >)^2}}, \tag{6}$$

https://doi.org/10.3390/universe12090261

where $< x >= \frac{\sum_{i=1}^{n} x_i}{n}$ and $< y >= \frac{\sum_{i=1}^{n} y_i}{n}$ are the mean values of the parameters $x$ and $y$. The Pearson correlation coefficient, $R(x, y)$, changes from $-1$ to $+1$, being a statistical measure of a linear correlation between two sets of data. The $R(x, y) = \pm 1$ values denote a perfect linear dependence between parameters $x$ and $y$ with all data points $(x_i, y_i)$ lying on a line in the $XY$ plane. The $R(x, y) = 0$ value implies an absence of a linear correlation between parameters $x$ and $y$. The positive and negative values of $R(x, y)$ show the positive and negative (linear) correlation, respectively, between parameters $x$ and $y$.

To evaluate the uncertainty in the $R(x, y)$ values, the standard error of the Pearson correlation coefficient is calculated as follows:

$$s_r = \sqrt{\frac{1 - R^2(x, y)}{n - 2}}. \quad (7)$$

The formula in Equation (7) is obtained under the assumption that the data are normally distributed and with the null hypothesis that there is a zero correlation between $x$ and $y$.

In the present work, we analyze the midrapidity $p_{\mathrm{T}}$ spectra of the charged pions and kaons, protons and antiprotons at seven multiplicity classes (see Table 1) in $p$+Pb collisions at $\sqrt{s_{nn}}$ = 5.02 TeV at the LHC, measured [43] by the ALICE collaboration, using the THMTF function presented in Equation (5). References [65,66] state that analyzing a single particle species via model fits fails to yield physically meaningful collective properties, including kinetic freeze-out temperature and radial transverse flow velocity. In contrast, extracting collective parameters like global freeze-out temperature and average transverse flow velocity becomes physically meaningful when performing simultaneous fits to various particle species produced in a collision [65,66]. Simultaneously fitting pion, kaon, proton, and antiproton spectra allows for an efficient comparison of different collision systems using only a few parameters [33,34,45–48,65,66]. In the present analysis, simultaneous minimum $\chi^2$ fits using the THMTF function (Equation (5)) were applied to the transverse momentum spectra of charged pions and kaons, protons and antiprotons across each centrality class in $p$+Pb collisions at $\sqrt{s_{nn}}$ = 5.02 TeV. This procedure was executed using the Nonlinear Curve Fitting package within Origin 9.1 Data Analysis and Graphing Software. During the simultaneous fitting procedure, the parameters $T_0$, $<\beta_{\mathrm{T}}>$, and $P_0$ were treated as global (shared) variables across all analyzed particle species. Error bars depicted in the figures of the present work show the combined (added) statistical and systematic uncertainties. This total uncertainty is mostly dominated by systematic components, which are significantly larger than the statistical ones. Minimum $\chi^2$ fits were executed by weighting each experimental data point by the inverse square of its combined uncertainty, $(1/(\text{combined error})^2)$. Following the approach in Refs. [45–48,64,66], the low-transverse-momentum region of $p_{\mathrm{T}} < 0.5$ GeV/$c$ for charged pions was excluded from the fitting procedure. This exclusion is a standard, commonly accepted procedure [65,66] because the low $p_{\mathrm{T}} < 0.5$ GeV/$c$ region contains a significant fraction of pions originating from baryon resonance decays. The simultaneously fitted $p_T$ ranges have been as follows: [0.5–20.0] GeV/$c$ for $\pi^+ + \pi^-$, [0.2–20.0] GeV/$c$ for $K^+ + K^-$, and [0.3–20.0] GeV/$c$ for $p$+$\overline{p}$.

## 3. Analysis and Results

The parameters obtained from simultaneous fits with the two-component model (THMTF) function (Equation (5)) of experimental midrapidity $p_T$ spectra of the charged pions and kaons, protons and antiprotons in seven multiplicity classes in $p$+Pb collisions at $\sqrt{s_{nn}}$ = 5.02 TeV using the fixed $x_{thr}$ = 5 GeV/$c$ parameter value are presented in Table 2. The corresponding minimum $\chi^2$ simultaneous fit curves of experimental midrapidity $p_T$ spectra of the studied particle species in all seven analyzed centrality classes of $p$+Pb

collisions at $\sqrt{s_{nn}}$ = 5.02 TeV are shown in Figure 1. As seen from Figure 1 and $\chi^2/n.d.f.$ values in Table 2, the THMTF function in Equation (5) describes quite well the experimental midrapidity $p_T$ spectra of the charged pions and kaons, protons and antiprotons in the whole measured $p_T$ range up to 20 GeV/$c$ at all seven multiplicity classes in $p$+Pb collisions at $\sqrt{s_{nn}}$ = 5.02 TeV. To perform the stability check and show that varying the $x_{thr}$ parameter does not shift significantly the extracted parameters and their $\langle N_{part} \rangle$ dependencies, we performed simultaneous fits with a two-component model (THMTF) function of experimental midrapidity $p_T$ spectra of the charged pions and kaons, protons and antiprotons in seven multiplicity classes in $p$+Pb collisions at $\sqrt{s_{nn}}$ = 5.02 TeV using also the fixed $x_{thr} = 5 \pm 1$ GeV/$c$ parameter values. The corresponding parameters of the THMTF function, obtained using the fixed $x_{thr}$ = 4 GeV/$c$ and $x_{thr}$ = 6 GeV/$c$ parameter values, are presented in Table 3.

**Table 2.** The results obtained from minimum $\chi^2$ simultaneous fits with a two-component model (THMTF) function (Equation (5)) of experimental midrapidity $p_T$ spectra of the charged pions and kaons, protons and antiprotons in different centrality classes of p+Pb collisions at $\sqrt{s_{nn}}$ = 5.02 TeV using the fixed $x_{thr}$ = 5 GeV/$c$ parameter value.

| Centrality ($\langle N_{part} \rangle$) | $\langle \beta_T \rangle$ | $T_0$, (MeV) | $P_0$, GeV/c | $q(\pi^{\pm})$ | $q(K^{\pm})$ | $q(p,\bar{p})$ | $n(\pi^{\pm})$ | $n(K^{\pm})$ | $n(p,\bar{p})$ | $\chi^2/n.d.f.$ ($n.d.f.$) |
|---|---|---|---|---|---|---|---|---|---|---|
| 0–5% (15.1 ± 0.75) | 0.39 ± 0.01 | 93 ± 3 | 1.23 ±0.09 | 1.128 ± 0.002 | 1.132 ± 0.002 | 1.115 ± 0.001 | 6.30 ± 0.10 | 6.14 ± 0.10 | 7.33 ± 0.16 | 0.29 (125) |
| 5–10% (13.5 ± 0.7) | 0.36 ± 0.01 | 94 ± 3 | 1.21 ±0.08 | 1.131 ± 0.002 | 1.135 ± 0.002 | 1.117 ± 0.001 | 6.26 ± 0.09 | 6.08 ± 0.09 | 7.31 ± 0.16 | 0.26 (125) |
| 10–20% (12.2 ± 0.6) | 0.33 ± 0.01 | 93 ± 2 | 1.17 ±0.08 | 1.134 ± 0.001 | 1.138 ± 0.001 | 1.118 ± 0.001 | 6.15 ± 0.08 | 5.99 ± 0.08 | 6.88 ± 0.13 | 0.23 (125) |
| 20–40% (10.1 ± 0.5) | 0.28 ± 0.01 | 95 ± 2 | 1.14 ±0.08 | 1.138 ± 0.001 | 1.142 ± 0.001 | 1.121 ± 0.001 | 6.18 ± 0.07 | 6.07 ± 0.08 | 6.99 ± 0.12 | 0.20 (125) |
| 40–60% (7.4 ± 0.3) | 0.21 ± 0.01 | 95 ± 2 | 1.08 ±0.08 | 1.140 ± 0.001 | 1.145 ± 0.001 | 1.120 ± 0.001 | 6.13 ± 0.07 | 5.98 ± 0.07 | 6.62 ± 0.11 | 0.17 (125) |
| 60–80% (4.9 ± 0.1) | 0.09 ± 0.01 | 96 ± 2 | 1.01 ±0.07 | 1.145 ± 0.001 | 1.152 ± 0.001 | 1.124 ± 0.001 | 6.10 ± 0.06 | 5.88 ± 0.05 | 6.53 ± 0.09 | 0.09 (125) |
| 80–100% (2.99 ± 0.03) | $\approx 10^{-12}$ | 87 ± 2 | 0.99 ±0.07 | 1.147 ± 0.001 | 1.152 ± 0.001 | 1.120 ± 0.001 | 5.91 ± 0.08 | 6.04 ± 0.08 | 6.60 ± 0.05 | 0.19 (125) |

**Table 3.** The same as in Table 2 obtained using the fixed $x_{thr}$ = 4 GeV/$c$ and $x_{thr}$ = 6 GeV/$c$ parameter values.

| Centrality | $\langle \beta_T \rangle$ | $T_0$, (MeV) | $P_0$, GeV/c | $q(\pi^{\pm})$ | $q(K^{\pm})$ | $q(p,\bar{p})$ | $n(\pi^{\pm})$ | $n(K^{\pm})$ | $n(p,\bar{p})$ | $\chi^2/n.d.f.$ ($n.d.f.$) |
|---|---|---|---|---|---|---|---|---|---|---|
| 0–5% ($x_{thr}$ = 4 GeV/$c$) | 0.37 ± 0.02 | 94 ± 3 | 1.24 ±0.10 | 1.129 ± 0.002 | 1.135 ± 0.002 | 1.120 ± 0.002 | 6.29 ± 0.06 | 6.11 ± 0.07 | 7.32 ± 0.10 | 0.25 (125) |
| 0–5% ($x_{thr}$ = 6 GeV/$c$) | 0.40 ± 0.02 | 92 ± 2 | 1.22 ±0.09 | 1.128 ± 0.002 | 1.131 ± 0.002 | 1.112 ± 0.002 | 6.24 ± 0.16 | 6.10 ± 0.14 | 7.16 ± 0.24 | 0.32 (125) |
| 5–10% ($x_{thr}$ = 4 GeV/$c$) | 0.34 ± 0.02 | 95 ± 3 | 1.21 ±0.09 | 1.132 ± 0.002 | 1.137 ± 0.002 | 1.122 ± 0.003 | 6.22 ± 0.06 | 6.06 ± 0.07 | 7.28 ± 0.10 | 0.23 (125) |
| 5–10% ($x_{thr}$ = 6 GeV/$c$) | 0.37 ± 0.01 | 93 ± 2 | 1.20 ±0.08 | 1.130 ± 0.002 | 1.134 ± 0.002 | 1.114 ± 0.002 | 6.29 ± 0.15 | 6.07 ± 0.14 | 7.20 ± 0.25 | 0.30 (125) |
| 10–20% ($x_{thr}$ = 4 GeV/$c$) | 0.31 ± 0.02 | 95 ± 3 | 1.17 ±0.09 | 1.135 ± 0.002 | 1.140 ± 0.002 | 1.123 ± 0.002 | 6.13 ± 0.05 | 5.99 ± 0.06 | 6.91 ± 0.08 | 0.19 (125) |
| 10–20% ($x_{thr}$ = 6 GeV/$c$) | 0.35 ± 0.02 | 92 ± 2 | 1.16 ±0.08 | 1.133 ± 0.001 | 1.136 ± 0.002 | 1.115 ± 0.002 | 6.12 ± 0.14 | 6.00 ± 0.12 | 6.76 ± 0.20 | 0.27 (125) |
| 20–40% ($x_{thr}$ = 4 GeV/$c$) | 0.26 ± 0.02 | 96 ± 3 | 1.11 ±0.10 | 1.138 ± 0.002 | 1.144 ± 0.002 | 1.125 ± 0.002 | 6.15 ± 0.05 | 6.02 ± 0.05 | 7.03 ± 0.07 | 0.16 (125) |

**Table 3.** *Cont.*

| Centrality | $\langle\beta_T\rangle$ | $T_0$, (MeV) | $P_0$, GeV/c | $q(\pi^{\pm})$ | $q(K^{\pm})$ | $q(p,\bar{p})$ | $n(\pi^{\pm})$ | $n(K^{\pm})$ | $n(p,\bar{p})$ | $\chi^2/n.d.f.$ ($n.d.f.$) |
|---|---|---|---|---|---|---|---|---|---|---|
| 20–40% ($x_{thr}$ = 6 GeV/$c$) | 0.30 ± 0.02 | 94 ± 2 | 1.10 ±0.09 | 1.136 ± 0.001 | 1.141 ± 0.001 | 1.117 ± 0.002 | 6.17 ± 0.12 | 6.12 ± 0.10 | 6.81 ± 0.20 | 0.24 (125) |
| 40–60% ($x_{thr}$ = 4 GeV/$c$) | 0.20 ± 0.01 | 95 ± 3 | 1.06 ±0.08 | 1.141 ± 0.001 | 1.147 ± 0.002 | 1.123 ± 0.001 | 6.08 ± 0.05 | 5.94 ± 0.05 | 6.68 ± 0.07 | 0.14 (125) |
| 40–60% ($x_{thr}$ = 6 GeV/$c$) | 0.22 ± 0.01 | 94 ± 2 | 1.05 ±0.09 | 1.140 ± 0.001 | 1.145 ± 0.001 | 1.119 ± 0.001 | 6.13 ± 0.11 | 5.97 ± 0.10 | 6.51 ± 0.18 | 0.18 (125) |
| 60–80% ($x_{thr}$ = 4 GeV/$c$) | 0.08 ± 0.01 | 95 ± 2 | 1.01 ±0.08 | 1.146 ± 0.001 | 1.154 ± 0.002 | 1.126 ± 0.002 | 6.06 ± 0.04 | 5.87 ± 0.04 | 6.62 ± 0.06 | 0.08 (125) |
| 60–80% ($x_{thr}$ = 6 GeV/$c$) | 0.10 ± 0.01 | 96 ± 2 | 1.01 ±0.08 | 1.144 ± 0.001 | 1.151 ± 0.001 | 1.122 ± 0.002 | 6.12 ± 0.09 | 5.91 ± 0.08 | 6.42 ± 0.14 | 0.10 (125) |
| 80–100% ($x_{thr}$ = 4 GeV/$c$) | $\approx 10^{-12}$ | 80 ± 3 | 0.90 ±0.10 | 1.153 ± 0.002 | 1.158 ± 0.001 | 1.124 ± 0.001 | 5.96 ± 0.05 | 5.97 ± 0.06 | 6.82 ± 0.15 | 0.10 (125) |
| 80–100% ($x_{thr}$ = 6 GeV/$c$) | $\approx 10^{-12}$ | 80 ± 3 | 0.88 ±0.12 | 1.152 ± 0.001 | 1.158 ± 0.001 | 1.125 ± 0.001 | 5.77 ± 0.12 | 6.11 ± 0.10 | 6.20 ± 0.22 | 0.09 (125) |

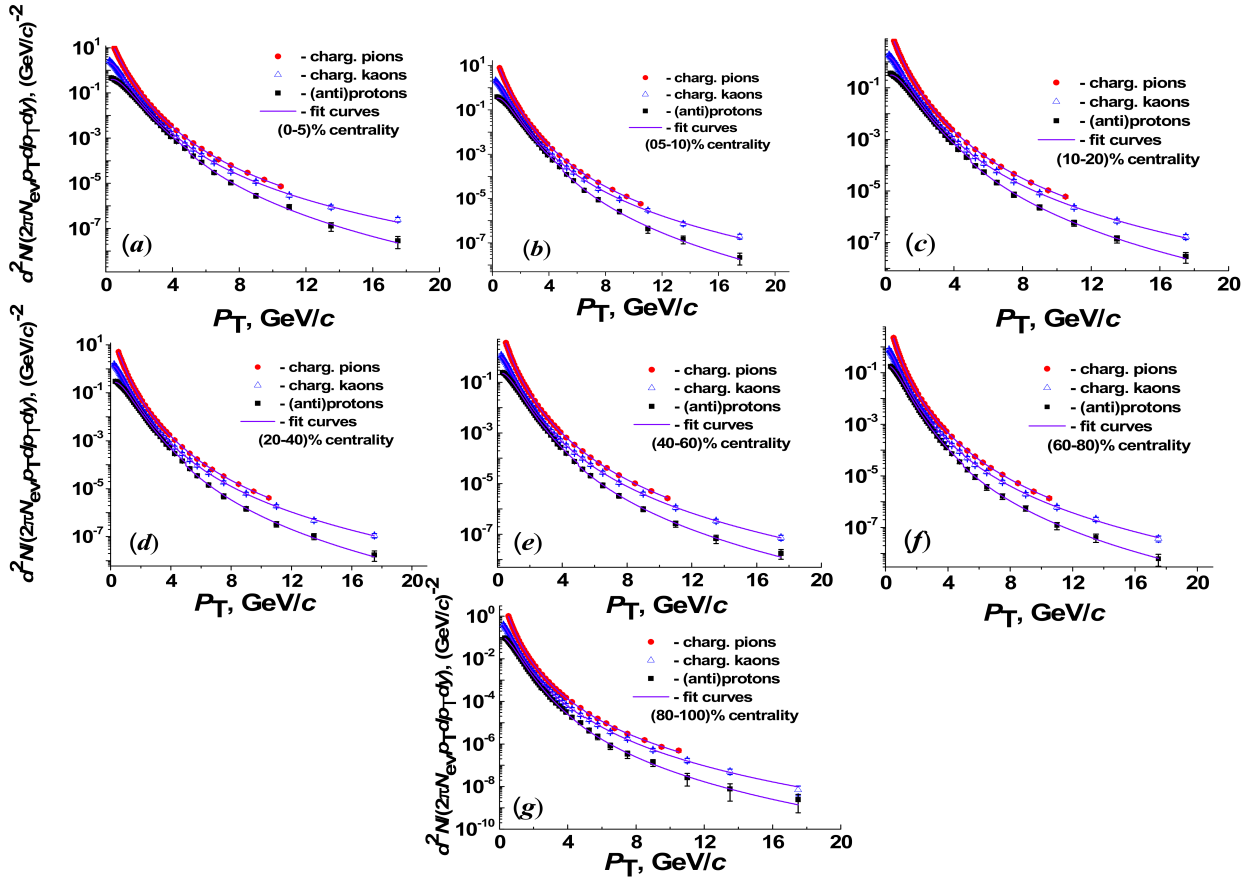



**Figure 1.** Simultaneous minimum $\chi^2$ fits (solid blue curves) with two-component model (THMTF) function (Equation (5)) of experimental midrapidity $p_T$ spectra (symbols) of the charged pions and kaons, protons and antiprotons in different centrality classes of $p$+Pb collisions at $\sqrt{s_{nn}}$ = 5.02 TeV: (**a**)—(0–5)%, (**b**)—(05–10)%, (**c**)—(10–20)%, (**d**)—(20–40)%, (**e**)—(40–60)%, (**f**)—(60–80)%, and (**g**)—(80–100)% centrality.

The dependencies of the obtained parameters $T_0$, $< \beta_T >$, and $q$ of two-component model (THMTF) function (Equation (5)), given in Table 2, on the average number of

participant nucleons ($\langle N_{part} \rangle$) in $p$+Pb collisions at $\sqrt{s_{nn}}$ = 5.02 TeV are illustrated in Figure 2. The dependencies of the obtained parameters $P_0$ and $n$ of the two-component THMTF function, given in Table 2, on $\langle N_{part} \rangle$ in $p$+Pb collisions at $\sqrt{s_{nn}}$ = 5.02 TeV are demonstrated in Figure 3. It is necessary to mention that varying the fixed $x_{thr}$ = 5 GeV/$c$ parameter value by ±1 GeV/$c$, as seen from comparison of Tables 2 and 3, shift most of the extracted parameters within their fitting uncertainties only and, therefore, practically does not change the $\langle N_{part} \rangle$ dependencies and trends of the parameters $T_0$, $< \beta_T >$, $q$, $P_0$, and $n$ observed in Figures 2 and 3. The dependencies of the extracted parameters $T_0$, $< \beta_T >$, $q$, $P_0$, and $n$ of two-component model (THMTF) function (Equation (5)), given in Table 2, on the average pseudorapidity density of the number of charged particles ($\langle dN_{ch}/d\eta \rangle$) in $p$+Pb collisions at $\sqrt{s_{nn}}$ = 5.02 TeV are shown in Figure 4. The dependencies of the parameters $q$, $T_0$, $P_0$, and $n$ on $\langle N_{part} \rangle$, obtained in Ref. [50] from minimum $\chi^2$ fits with two-component THMTF function of the experimental $p_T$ spectra of the primary charged particles at nine centrality classes in Pb+Pb collisions at $\sqrt{s_{nn}}$ = 2.76 and 5.02 TeV, are presented in Figure 5 for a comparison. Pearson correlation coefficients, $R(x, y)$, between various parameters of two-component THMTF function, extracted in present work from simultaneous minimum $\chi^2$ fits of experimental midrapidity $p_T$ spectra of the charged pions and kaons, protons and antiprotons in $p$+Pb collisions at $\sqrt{s_{nn}}$ = 5.02 TeV and given in Table 2, are presented in Table 4. The corresponding Pearson correlation coefficients, $R(x, y)$, between various parameters of two-component THMTF function, obtained in Ref. [50] from minimum $\chi^2$ fits of experimental midrapidity $p_T$ spectra of primary charged particles in Pb+Pb collisions at $\sqrt{s_{nn}}$ = 2.76 and 5.02 TeV, are shown in Table 5 for a comparison. The two-tailed $p$-values, determined from Student's $t$-test with the null hypothesis that there is a zero correlation between parameters $x$ and $y$ ($R(x, y) = 0$), are also given for each $R(x, y)$ value in Tables 4 and 5. To test the null hypothesis, the alpha level (significance threshold), $\alpha = 0.05$, which corresponds to a 95% confidence level, is usually set. If $p \leq \alpha$ ($p \leq 0.05$), the null hypothesis gets rejected, and the result is statistically significant. On the contrary, if $p > \alpha$ ($p > 0.05$), one fails to reject the null hypothesis, and the result is statistically insignificant.

**Table 4.** Pearson correlation coefficient, $R(x, y)$, and its corresponding standard error between various parameters of the two-component model function (Equation (5)), extracted from combined minimum $\chi^2$ fits of experimental midrapidity transverse momentum spectra of the charged pions and kaons, protons and antiprotons in $p$+Pb collisions at $\sqrt{s_{nn}}$ = 5.02 TeV and given in Table 2. The corresponding two-tailed $p$-value is given inside round brackets below each $R(x, y)$ value (for *n.d.f.* = 6).

| $R(x, y)$ | Value | $R(x, y)$ | Value |
|---|---|---|---|
| $R(<\beta_T>, T_0)$ | +0.44 ± 0.40 (0.3135) | $R(q, <\beta_T>)$ (for pions) | –0.97 ± 0.11 (0.000118) |
| $R(<\beta_T>, P_0)$ | +0.98 ± 0.08 (0.000018) | $R(q, <\beta_T>)$ (for kaons) | –0.97 ± 0.11 (0.000118) |
| $R(P_0, T_0)$ | +0.30 ± 0.43 (0.5115) | $R(q, <\beta_T>)$ (for (anti)protons) | –0.73 ± 0.31 (0.0567) |
| $R(P_0, <N_{part}>)$ | +0.99 ± 0.04 (0.00000029) | $R(q, <N_{part}>)$ (for pions) | –0.99 ± 0.05 (0.0000011) |
| $R(<\beta_T>, <N_{part}>)$ | +0.99 ± 0.08 (0.000017) | $R(q, <N_{part}>)$ (for kaons) | –0.99 ± 0.06 (0.00000316) |
| $R(T_0, <N_{part}>)$ | +0.33 ± 0.42 (0.4618) | $R(q, <N_{part}>)$ (for (anti)protons) | –0.80 ± 0.27 (0.0252) |
| $R(<\beta_T>, n)$ (for pions) | +0.93 ± 0.17 (0.0016) | $R(P_0, n)$ (for pions) | +0.90 ± 0.20 (0.0041) |

**Table 4.** *Cont.*

| $R(x, y)$ | Value | $R(x, y)$ | Value |
|---|---|---|---|
| $R(<\beta_T>, n)$ (for kaons) | +0.57 ± 0.37 (0.1745) | $R(P_0, n)$ (for kaons) | +0.68 ± 0.33 (0.0851) |
| $R(<\beta_T>, n)$ (for (anti)protons) | +0.86 ± 0.23 (0.00963) | $R(P_0, n)$ (for (anti)protons) | +0.93 ± 0.16 (0.0011) |
| $R(q, T_0)$ (for pions) | –0.28 ± 0.43 (0.5398) | $R(n, T_0)$ (for pions) | +0.63 ± 0.35 (0.122) |
| $R(q, T_0)$ (for kaons) | –0.22 ± 0.44 (0.6349) | $R(n, T_0)$ (for kaons) | –0.31 ± 0.42 (0.4929) |
| $R(q, T_0)$ (for (anti)protons) | +0.24 ± 0.43 (0.5970) | $R(n, T_0)$ (for (anti)protons) | +0.12 ± 0.44 (0.794) |
| $R(q, P_0)$ (for pions) | –0.99 ± 0.07 (0.00000781) | $R(n, <N_{part}>)$ (for pions) | +0.91 ± 0.18 (0.00232) |
| $R(q, P_0)$ (for kaons) | –0.99 ± 0.05 (0.0000011) | $R(n, <N_{part}>)$ (for kaons) | +0.64 ± 0.34 (0.1089) |
| $R(q, P_0)$ (for (anti)protons) | –0.81 ± 0.26 (0.0207) | $R(n, <N_{part}>)$ (for (anti)protons) | +0.92 ± 0.18 (0.0022) |

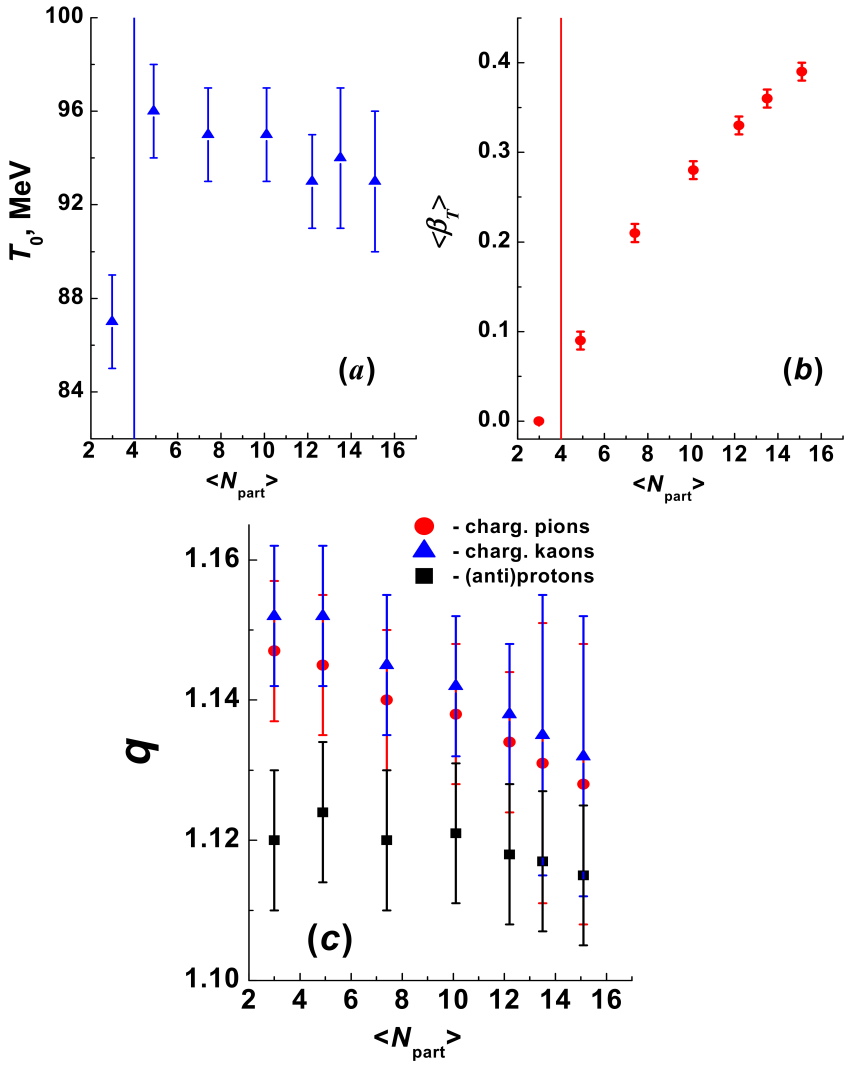



**Figure 2.** The dependencies of the obtained parameters $T_0$ (**a**), $< \beta_T >$ (**b**), and $q$ (**c**) of the two-component model (THMTF) function (Equation (5)), given in Table 2, on the average number of participant nucleons ($\langle N_{part} \rangle$) in $p$+Pb collisions at $\sqrt{s_{nn}}$ = 5.02 TeV. The vertical lines in panels (**a**) and (**b**).

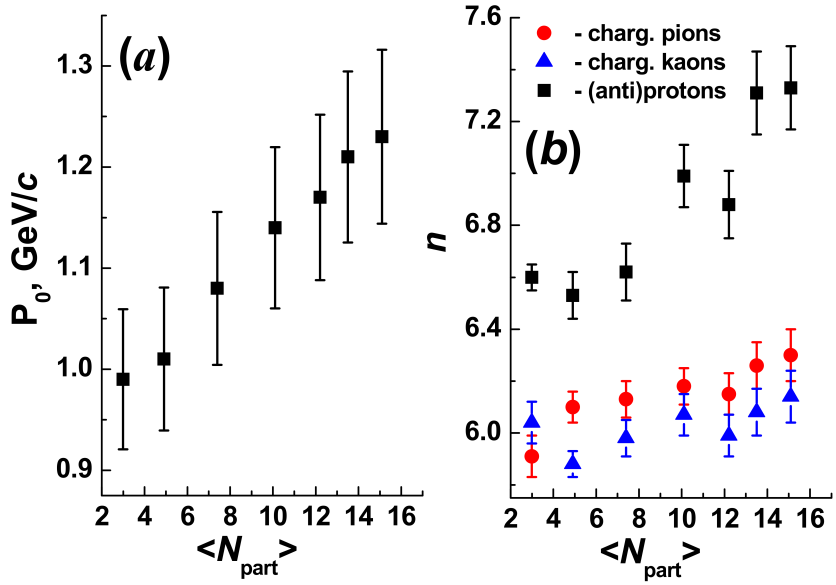



**Figure 3.** The dependencies of the obtained parameters $P_0$ (**a**) and $n$ (**b**) of the two-component model (THMTF) function (Equation (5)), given in Table 2, on the average number of participant nucleons ($\langle N_{part} \rangle$) in $p$+Pb collisions at $\sqrt{s_{nn}}$ = 5.02 TeV.

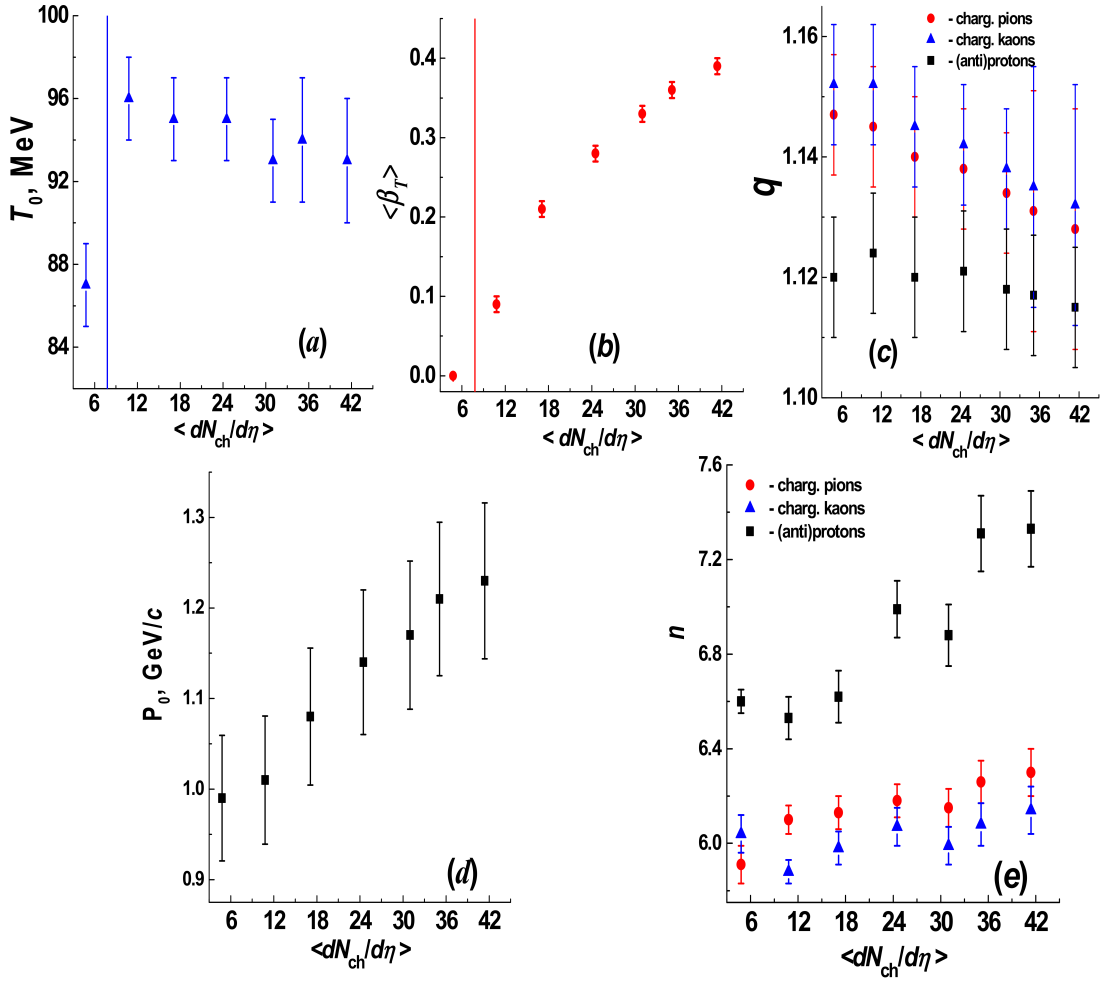



**Figure 4.** The dependencies of the obtained parameters $T_0$ (**a**), $< \beta_T >$ (**b**), $q$ (**c**), $P_0$ (**d**) and $n$ (**e**) of the two-component model (THMTF) function (Equation (5)), given in Table 2, on $\langle dN_{ch}/d\eta \rangle$ in $p$+Pb collisions at $\sqrt{s_{nn}}$ = 5.02 TeV.

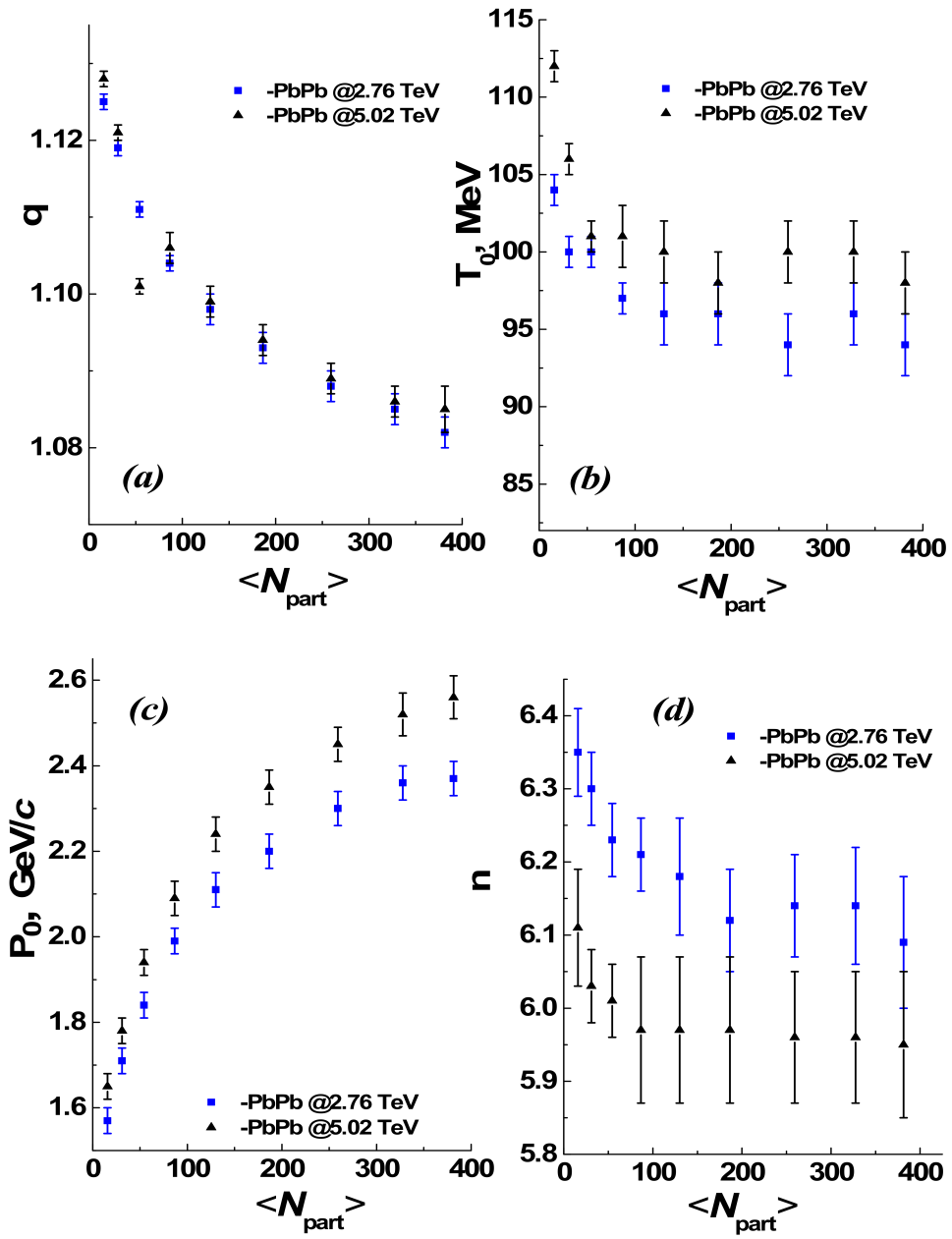



**Figure 5.** The dependencies of the parameters $q$ (**a**), $T_0$ (**b**), $P_0$ (**c**), and $n$ (**d**) on the average number of participant nucleons ($\langle N_{part} \rangle$), obtained in Ref. [50] from minimum $\chi^2$ fits with a two-component model (THMTF) function of the experimental transverse momentum spectra of the primary charged particles at nine centrality classes in Pb+Pb collisions at $\sqrt{s_{nn}}$ = 2.76 and 5.02 TeV.

Figure 2b shows that the transverse flow velocity is initially absent at the first data point, which corresponds to the 80–100% centrality interval of $p$+Pb collisions. Beyond this point, the average transverse velocity, $< \beta_T >$, emerges and increases monotonically with growing collision centrality, represented by $\langle N_{part} \rangle$. At the same time, Figure 2a indicates that the kinetic freeze-out temperature $T_0$ rises with $\langle N_{part} \rangle$ up to approximately $\langle N_{part} \rangle \approx 4$, after which it remains constant within the experimental uncertainties in the region $\langle N_{part} \rangle > 4$. A closer inspection of Figure 2b reveals that while the transverse flow velocity is zero at the first point $\langle N_{part} \rangle = 2.99$, it becomes statistically noticeable ($< \beta_T > \approx 0.1$) by the second point $\langle N_{part} \rangle = 4.9$. Consequently, the threshold value for the onset of collective transverse radial flow in $p$+Pb collisions at $\sqrt{s_{nn}}$ = 5.02 TeV is estimated to be $\langle N_{part} \rangle \approx 4.0 \pm 0.5$. This boundary is determined as the midpoint in $\langle N_{part} \rangle$ between the first and second data points in Figure 2b, which correspond to the 80–100% and

60–80% centrality classes listed in Table 1, respectively. The uncertainty (±0.5) is estimated, similarly to Ref. [45], as the half-width between the midpoint value of 4.0 and central values of the centrality bins 80–100% ($\langle N_{part} \rangle$ = 2.99) and 60–80% ($\langle N_{part} \rangle$ = 4.9). This boundary value, $\langle N_{part} \rangle \approx 4.0 \pm 0.5$, estimated in present work from analysis of $\langle N_{part} \rangle$ dependencies of the parameters $< \beta_{\mathrm{T}} >$ and $T_0$ of the two-component model (THMTF) function (Equation (5)), has coincided with the corresponding boundary $\langle N_{part} \rangle$ value, evaluated in Ref. [45] from simultaneous analysis of midrapidity $p_T$ distributions of the charged pions and kaons, protons and antiprotons in $p$+Pb collisions at $\sqrt{s_{nn}}$ = 5.02 TeV in region $p_T \leq 0.5$ GeV/$c$, using thermodynamically consistent Tsallis function with embedded transverse flow (Equation (2)). Simultaneous analyses of $< \beta_{\mathrm{T}} >$, $T_0$ and $q$ as functions of $\langle N_{part} \rangle$ in Refs. [46–48] have suggested that these boundary $\langle N_{part} \rangle$ values reflect not only the onset of transverse radial flow, but possibly also the threshold for a possible crossover phase transition from a dense hadronic state to a QGP. Indications of this possible transition threshold have been observed across several collision systems and energies at the LHC, including Xe+Xe collisions at $\sqrt{s_{nn}}$ = 5.44 TeV [46], as well as Pb+Pb collisions at $\sqrt{s_{nn}}$ = 2.76 TeV [48] and $\sqrt{s_{nn}}$ = 5.02 TeV [47]. The corresponding threshold values have been estimated to be $\langle N_{part} \rangle \approx 44 \pm 5$, $71 \pm 5$, and $71 \pm 7$ in Xe+Xe collisions at $\sqrt{s_{nn}}$ = 5.44 TeV [46], Pb+Pb collisions at $\sqrt{s_{nn}}$ = 2.76 TeV [48], and Pb+Pb collisions at $\sqrt{s_{nn}}$ = 5.02 TeV [47], respectively.

**Table 5.** Pearson correlation coefficient, $R(x, y)$, and its corresponding standard error between various parameters of the two-component model function (Equation (5)), obtained in Ref. [50] from minimum $\chi^2$ fits of experimental midrapidity transverse momentum spectra of primary charged particles in Pb+Pb collisions at $\sqrt{s_{nn}}$ = 2.76 and 5.02 TeV. The corresponding two-tailed $p$-value is given inside round brackets below each $R(x, y)$ value (for *n.d.f.* = 8).

| Collision Type | Pb+Pb Collisions at $\sqrt{s_{nn}}$ = 2.76 TeV | Pb+Pb Collisions at $\sqrt{s_{nn}}$ = 5.02 TeV |
|---|---|---|
| $R(<\beta_{\mathrm{T}}>, T_0)$ | $-0.97 \pm 0.09$ (0.00000484) | $-0.95 \pm 0.12$ (0.000047) |
| $R(<\beta_{\mathrm{T}}>, P_0)$ | $+0.99 \pm 0.06$ (0.000000184) | $+0.97 \pm 0.10$ (0.0000107) |
| $R(P_0, T_0)$ | $-0.95 \pm 0.12$ (0.000047) | $-0.85 \pm 0.20$ (0.00280) |
| $R(<\beta_{\mathrm{T}}>, n)$ | $-0.98 \pm 0.07$ (0.000000657) | $-0.97 \pm 0.10$ (0.0000107) |
| $R(q, T_0)$ | $+0.94 \pm 0.13$ (0.0000898) | $+0.91 \pm 0.16$ (0.000461) |
| $R(q, P_0)$ | $-0.99 \pm 0.02$ (0.0000000000307) | $-0.96 \pm 0.10$ (0.0000115) |
| $R(q, <\beta_{\mathrm{T}}>)$ | $-0.98 \pm 0.07$ (0.000000657) | $-0.97 \pm 0.10$ (0.0000107) |
| $R(q, n)$ | $+0.97 \pm 0.09$ (0.00000484) | $+0.90 \pm 0.17$ (0.00073) |
| $R(q, <N_{part}>)$ | $-0.94 \pm 0.13$ (0.0000898) | $-0.88 \pm 0.18$ (0.001211) |
| $R(P_0, n)$ | $-0.97 \pm 0.09$ (0.00000484) | $-0.89 \pm 0.17$ (0.000788) |
| $R(P_0, <N_{part}>)$ | $+0.93 \pm 0.14$ (0.000162) | $+0.94 \pm 0.13$ (0.0000898) |
| $R(n, T_0)$ | $+0.94 \pm 0.13$ (0.0000898) | $+0.96 \pm 0.11$ (0.0000232) |
| $R(n, <N_{part}>)$ | $-0.87 \pm 0.19$ (0.00180) | $-0.73 \pm 0.26$ (0.02292) |

The threshold $\langle N_{part} \rangle$ values for Pb+Pb collisions at $\sqrt{s_{nn}}$ = 2.76 TeV [48] and 5.02 TeV [47] are significantly higher than those observed in Xe+Xe collisions [46] at $\sqrt{s_{nn}}$ = 5.44 TeV. As noted in Refs. [47,48], this difference is likely due to the larger mass number ($A$) of Pb relative to Xe, implying that the greater nuclear size naturally yields a higher number of participant nucleons within the overlap zone, even though the threshold in both systems corresponds to a similar centrality range (between the 40–50% and 50–60% centrality classes). Conversely, the consistency of the threshold $\langle N_{part} \rangle$ values between the two Pb+Pb collision energies can be attributed to the identical collision system and geometry [48].

In contrast, the threshold value of $\langle N_{part} \rangle \approx 4.0 \pm 0.5$ estimated for $p$+Pb collisions at $\sqrt{s_{nn}}$ = 5.02 TeV in the present work is substantially smaller than those reported earlier for the heavier Xe+Xe [46] and Pb+Pb [47,48] collision systems at the LHC. This difference is expected due to the considerably smaller overlap volume and the resulting lower number of participant nucleons in asymmetric $p$+Pb collisions compared to symmetric nucleus-nucleus (Pb+Pb) systems.

Interestingly, the behavior of the freeze-out temperature $T_0$ as a function of $\langle N_{part} \rangle$ (or collision centrality) in $p$+Pb collisions at $\sqrt{s_{nn}}$ = 5.02 TeV (Figure 2a) closely resembles the $T_0$ dependence on midrapidity charged-particle multiplicity density ($\langle dN_{ch}/d\eta \rangle$) previously observed [33,34] in p+p collisions at $\sqrt{s}$ = 7 and 13 TeV. In both small systems, $T_0$ initially rises up to the threshold $\langle N_{part} \rangle$ value and subsequently stabilizes within uncertainties, exhibiting a distinct plateau-like behavior at higher multiplicities [33,34]. This initial increase in $T_0$ in small systems can be attributed to higher initial energy density and intense partonic hard scattering in higher-multiplicity events, which creates a hotter system that decouples rapidly before undergoing significant expansion and cooling.

In contrast, nucleus-nucleus ($A$+$A$) collisions display a fundamentally different trend, as recently reported for Xe+Xe collisions at $\sqrt{s_{nn}}$ = 5.44 TeV [46], Pb+Pb collisions at $\sqrt{s_{nn}}$ = 2.76 TeV [48], and Pb+Pb collisions at $\sqrt{s_{nn}}$ = 5.02 TeV [47]. In these heavy-ion systems, $T_0$ initially decreases up to the threshold $\langle N_{part} \rangle$ value before flattening into a plateau in the more central region [46–48]. This behavior can be seen also in Figure 5b, where the $\langle N_{part} \rangle$ dependence of $T_0$, obtained in Ref. [50] from minimum $\chi^2$ fits with two-component THMTF function of the experimental $p_T$ spectra of the primary charged particles in Pb+Pb collisions at $\sqrt{s_{nn}}$ = 2.76 and 5.02 TeV, is presented. This contrasting behavior can be understood through a geometric and expansion-driven mechanism: in large nuclear systems, more central collisions lead to a larger initial volume and stronger collective radial flow. The resulting prolonged hydrodynamic expansion phase allows the system to cool down more extensively before reaching the low-density decoupling limit, effectively lowering the kinetic freeze-out temperature $T_0$ before it stabilizes in more central events.

Figure 2c shows that the non-extensivity parameter $q$ consistently decreases across all analyzed particle species as the centrality (or $\langle N_{part} \rangle$) of $p$+Pb collisions at $\sqrt{s_{nn}}$ = 5.02 TeV increases. This decreasing trend of $q$ can also be seen in Figure 5a, where the $\langle N_{part} \rangle$ dependence of parameter $q$, obtained in Ref. [50] from minimum $\chi^2$ fits with a two-component THMTF function of the experimental $p_T$ spectra of the primary charged particles in Pb+Pb collisions at $\sqrt{s_{nn}}$ = 2.76 and 5.02 TeV, is shown. It is worth noting that a slight deviation/irregularity is visible for one of the data points in Pb+Pb collisions at $\sqrt{s_{nn}}$ = 5.02 TeV in Figure 5a. This localized deviation in the peripheral-to-intermediate centrality transition region ($\langle N_{part} \rangle \approx$ 50–70) could be attributed to significant initial-state geometrical fluctuations, sensitivity to centrality selection estimators, and strong correlations (as seen in Table 5) between the freeze-out temperature, $T_0$, and the non-extensivity parameter, $q$, in peripheral heavy-ion collisions. This decline of $q$ implies that the degree of system

thermalization and statistical equilibrium increases in more central collisions, as evidenced by $q$ approaching unity (+1). Furthermore, the data reveal a clear hierarchy among particle species: $q$ (mesons) > $q$ ((anti)protons). While the $q$ values for kaons and pions remain close to each other, they are significantly higher than those for (anti)protons. This mass- or quark number-dependent ordering agrees well with the relation $q$ (baryons) < $q$ (mesons) observed previously [45–48,50,67] in high-energy collisions.

Physically, this hierarchy could be explained qualitatively in terms of quark coalescence and flavor dynamics. Baryons, composed of three constituent quarks, require a higher number of local partonic interactions to form compared to two-quark mesons. Consequently, baryons preferentially sample the denser, more frequently interacting, and highly thermalized core of the collision volume. This intensive interaction history could drive baryons closer to a classical Boltzmann-Gibbs thermal distribution, resulting in a lower $q$ value. In contrast, lighter mesons seem to be more affected by surface production and hard scattering. These processes could limit thermalization, increasing the $q$ parameter of mesons.

As illustrated in Figure 3a, the momentum scale parameter $P_0$ of the inverse power-law component in Equation (5) rises steadily with $\langle N_{part} \rangle$ for $p$+Pb collisions at $\sqrt{s_{nn}}$ = 5.02 TeV. This rise in $P_0$ stems from increased energy-momentum transfer and more frequent hard scatterings in more central collisions, which ultimately elevates the average $p_T$. Furthermore, comparing Figures 2b and 3a reveals that this continuous growth of $P_0$ closely tracks the onset and evolution of the average transverse flow velocity ($< \beta_T >$). This is supported by the strong positive correlation between parameters $< \beta_T >$ and $P_0$ with corresponding Pearson correlation coefficient, $R(<\beta_T>, P_0)$ = +0.98 ± 0.08, given in Table 4. This alignment confirms that more central $p$+Pb collisions generate stronger pressure gradients in the interaction zone, inducing a stronger transverse flow that pushes particles toward higher $p_T$ values.

As seen from Figure 3b, the power index $n$ for protons and antiprotons demonstrates a significant increase with $\langle N_{part} \rangle$ in $p$+Pb collisions at $\sqrt{s_{nn}}$ = 5.02 TeV, whereas parameter $n$ for pions and kaons, on the whole, shows a very weak increase with an increase in collision centrality, staying nearly constant within uncertainties. In contrast to $p$+Pb collisions, the power index $n$ for primary charged particles in Pb+Pb collisions at $\sqrt{s_{nn}}$ = 2.76 and 5.02 TeV in Figure 5d demonstrates a significant decrease with $\langle N_{part} \rangle$ in the region up to $\langle N_{part} \rangle \approx 100$, and then it stabilizes in the region $\langle N_{part} \rangle > 100$, showing a very slight decrease or almost plateau-like behavior.

It is necessary to mention that the $\langle dN_{ch}/d\eta \rangle$ dependencies of the parameters $T_0$, $< \beta_T >$, $q$, $P_0$ and $n$ of the two-component model (THMTF) function (Equation (5)), demonstrated in Figure 4, are similar to and reflect fully the $\langle N_{part} \rangle$ dependencies of the corresponding parameters in $p$+Pb collisions at $\sqrt{s_{nn}}$ = 5.02 TeV, observed in Figures 2 and 3.

While the momentum scale parameter $P_0$ reflects the initial local energy density across these systems, the structural evolution of the hard-$p_T$ spectral tail, governed by the power index $n$, reveals a strong contrast in the underlying physics between $p$+Pb and Pb+Pb systems. Formally, the power index $n$ quantifies the rate of fall-off of the hard-$p_T$ tail, where a decreasing $n$ denotes spectral hardening due to hard partonic processes or collective dynamics, and an increasing $n$ indicates a softer spectral shape. In large-scale Pb+Pb collisions, central events generate a dense, strongly coupled Quark-Gluon Plasma (QGP) that induces immense hydrodynamic pressure gradients. This drives a powerful collective radial flow ($< \beta_T >$) that hydrodynamically shifts the bulk particle distribution toward higher $p_T$ region. More frequent hard partonic scatterings lead to an increase in the number of higher-$p_T$ hadrons with an increase in centrality of Pb+Pb collisions, which results in a spectral flattening, represented mathematically by a decreasing $n$ parameter, observed in

Figure 5d. In contrast, the $p$+Pb system is too small and light mesons form primarily via vacuum-like jet fragmentation in $p$+Pb collisions. Consequently, their spectral slope remains stable, yielding a negligible increase in $n$ with $\langle N_{part} \rangle$, as seen in Figure 3b. Meanwhile, protons and antiprotons seem to be strongly affected by non-perturbative processes like parton recombination or coalescence at intermediate $p_T$ values. This baryon enhancement can populate heavily the mid-$p_T$ region, leaving the higher hard-$p_T$ tail looking isolated and steeper. This can mathematically force a sharp increase in the fitted power index $n$ with an increase in $\langle N_{part} \rangle$, observed for protons and antiprotons in $p$+Pb collisions in Figure 3b.

The similarities and differences in the $\langle N_{part} \rangle$ dependencies of the parameters of the two-component THMTF function, observed in $p$+Pb collisions at $\sqrt{s_{nn}}$ = 5.02 TeV collisions in Figures 2 and 3 and Pb+Pb collisions at $\sqrt{s_{nn}}$ = 2.76 and 5.02 TeV in Figure 5, are reflected in the similarities and differences in the Pearson linear correlation coefficients between corresponding parameters, presented in Tables 4 and 5, respectively.

As seen from Table 4, in case of p+Pb collisions at $\sqrt{s_{nn}}$ = 5.02 TeV, pairs of parameters such as $<\beta_T>$ and $P_0$, $P_0$ and $<N_{part}>$, $<\beta_T>$ and $<N_{part}>$ show strong statistically significant correlations ($p << 0.05$), whereas pairs such as $<\beta_T>$ and $T_0$, $P_0$ and $T_0$, $T_0$ and $<N_{part}>$ are characterized by statistically insignificant correlations ($p > 0.05$) consistent with $R(x, y) = 0$. Whereas in case of Pb+Pb collisions at $\sqrt{s_{nn}}$ = 2.76 and 5.02 TeV, as seen from Table 5, all presented pairs of parameters demonstrate strong statistically significant correlations ($p << 0.05$). As seen from Tables 4 and 5, the correlation between parameters $< \beta_T >$ and $P_0$, as well as between parameters $P_0$ and $\langle N_{part} \rangle$, is strongly positive in both $p$+Pb collisions at $\sqrt{s_{nn}}$ = 5.02 TeV and Pb+Pb collisions at $\sqrt{s_{nn}}$ = 2.76 and 5.02 TeV. This is because both $< \beta_T >$ and $P_0$ rise with an increase in $\langle N_{part} \rangle$ in both p+Pb and Pb+Pb collisions, as seen in Figures 2, 3 and 5. On the other hand, the correlation between parameters $q$ and $P_0$, between parameters $q$ and $< \beta_T >$ and between parameters $q$ and $\langle N_{part} \rangle$, is strongly negative in both $p$+Pb and Pb+Pb collisions. It is due to the similar $\langle N_{part} \rangle$ dependencies of the parameters $q$, $P_0$, and $< \beta_T >$ observed in $p$+Pb collisions and Pb+Pb collisions in Figures 2, 3 and 5. As seen from Tables 4 and 5, the correlation between parameters $< \beta_T >$ and $n$ is significantly positive for pions and (anti)protons in $p$+Pb collisions, whereas it is strongly negative with $R(<\beta_T>, n) \approx -1$ in Pb+Pb collisions. This is due to opposite trends in $\langle N_{part} \rangle$ dependencies of power-index $n$ in $p$+Pb and Pb+Pb collisions, observed in Figures 3b and 5d: parameter $n$ on the whole increases with $\langle N_{part} \rangle$ in $p$+Pb collisions in Figure 3b, whereas $n$ generally decreases with an increase in $\langle N_{part} \rangle$ in Pb+Pb collisions in Figure 5d. Table 4 shows practically no correlation between parameters $q$ and $T_0$ in $p$+Pb collisions, whereas the correlation between these parameters is strongly positive with $R(q, T_0) \approx +0.9$ in Pb+Pb collisions in Table 5. This is, as discussed earlier, due to significant differences in the $\langle N_{part} \rangle$ dependencies of $T_0$ in $p$+Pb and Pb+Pb collisions, as seen in Figures 2a and 5b. The differences in the $R(x, y)$ values of other parameters in $p$+Pb collisions in the present work and Pb+Pb collisions in Ref. [50] (Tables 4 and 5) can be explained similarly. These discrepancies come from the corresponding differences observed in the $\langle N_{part} \rangle$ dependencies of either the kinetic freeze-out temperature parameter ($T_0$) or the power index ($n$) in $p$+Pb and Pb+Pb collision systems.

## 4. Summary and Conclusions

In this work, we have presented a comprehensive systematic analysis of the centrality ($\langle N_{part} \rangle$) dependencies of midrapidity transverse momentum ($p_T$) spectra for identified light-flavor hadrons—specifically charged pions and kaons, and protons/antiprotons in asymmetric $p$+Pb collisions at $\sqrt{s_{nn}}$ = 5.02 TeV. We have employed the new two-component Tsallis-Hagedorn Model with Transverse Flow (THMTF) to reproduce the experimental midrapidity $p_T$ spectra for identified light-flavor hadrons, measured by the ALICE collabo-

ration, across seven multiplicity classes, quantified by the average number of participant nucleons ($\langle N_{part} \rangle$), in $p$+Pb collisions at $\sqrt{s_{nn}}$ = 5.02 TeV. This two-component THMTF function is the sum of a thermodynamically consistent Tsallis function with embedded transverse flow and an inverse power-law function (which is asymptotic to the QCD-inspired Hagedorn function at high $p_{\mathrm{T}}$ values), which are assumed to describe the soft and hard $p_T$ components of transverse momentum spectrum, respectively. The extracted THMTF function parameters and their physical trends with an increase in $\langle N_{part} \rangle$ in asymmetric $p$+Pb collisions at $\sqrt{s_{nn}}$ = 5.02 TeV were systematically compared with those of symmetric Pb+Pb collisions at $\sqrt{s_{nn}}$ = 2.76 and 5.02 TeV.

The two-component THMTF model has successfully described the experimental transverse momentum distributions across the entire measured $p_T$ range up to 20 GeV/$c$. The high quality of the simultaneous fits of midrapidity $p_T$ spectra of identified light-flavor hadrons, evidenced by the $\chi^2/n.d.f.$ values, establishes this new two-component model as an efficient phenomenological tool capable of bridging the physics of small asymmetric and large symmetric collision systems using just a few parameters.

The systematic mapping of the fit parameters as a function of $\langle N_{part} \rangle$ has revealed key insights into the thermodynamic and collective properties of the media produced in high-energy collisions at the LHC. While collective radial flow is absent in peripheral p+Pb collisions at $\langle N_{part} \rangle$ = 2.99, it emerges at higher multiplicities. The threshold for the onset of collective transverse radial flow has been estimated to be $\langle N_{part} \rangle \approx 4.0 \pm 0.5$. This boundary is further supported by the $\langle N_{part} \rangle$ dependence of the kinetic freeze-out temperature $T_0$, which rises steadily with increasing centrality up to $\langle N_{part} \rangle \approx 4.0 \pm 0.5$ before transitioning into a stable, constant plateau region. This threshold, representing the onset of collective expansion in p+Pb collisions (and possibly the critical boundary for a crossover phase transition to a QGP), is substantially smaller than those reported earlier for symmetric systems ($\langle N_{part} \rangle \approx 44 \pm 5$ and $\approx 71 \pm 7$ in Xe+Xe and Pb+Pb collisions at the LHC, respectively). This scaling reflects the fundamental role of initial collision geometry, where smaller overlap volumes naturally require fewer participant nucleons to initiate collective behavior.

The kinetic freeze-out temperature parameter ($T_0$) exhibits fundamentally divergent trends between small and large collision systems. In $p$+Pb collisions, $T_0$ initially rises up to the threshold $\langle N_{part} \rangle$ value before stabilizing into a plateau, closely resembling the similar behavior observed in p+p collisions at $\sqrt{s}$ = 7 and 13 TeV at the LHC. This is driven by high initial energy densities and intense partonic hard scattering in high-multiplicity proton-proton events, causing the hot tiny-volume system to decouple rapidly before undergoing significant expansion. Conversely, heavy-ion systems (Pb+Pb and Xe+Xe) exhibit an initial decrease in $T_0$ due to a larger initial volume and a prolonged hydrodynamic expansion phase, which allows the medium to cool down extensively before reaching the low-density decoupling limit.

In both $p$+Pb and Pb+Pb collision systems, the non-extensivity parameter $q$ consistently decreases toward unity (+1) as centrality increases, qualitatively indicating enhanced thermalization and a transition toward classical Boltzmann-Gibbs statistical equilibrium in central collisions. The observed hierarchy, $q$(mesons) > $q$(baryons), could possibly reflect the differences in quark contents and corresponding production mechanisms of mesons and baryons qualitatively.

The momentum scale parameter ($P_0$) rises steadily with centrality in both $p$+Pb and Pb+Pb collisions, strongly correlating with the average flow velocity ($< \beta_{\mathrm{T}} >$) ($R(<\beta_{\mathrm{T}}>, P_0) \approx +1$). However, the power-index $n$, which governs the high-$p_T$ spectral tail, reveals a strong contrast in underlying physics of $p$+Pb and Pb+Pb systems. In large-scale Pb+Pb collisions, $n$ decreases with centrality (spectral flattening), which could be explained quali-

tatively by an increase in the number of hard partonic scatterings and produced higher-$p_T$ hadrons. In small-scale $p$+Pb collisions, $n$ remains nearly constant for light mesons (consistent with their production via vacuum-like jet fragmentation), but increases sharply for protons and antiprotons with an increase in $\langle N_{part} \rangle$. This increase in the parameter $n$ for protons and antiprotons could qualitatively reflect the well-known phenomenon of intermediate-$p_T$ baryon enhancement driven by non-perturbative parton recombination/coalescence, which increases with an increase in collision centrality.

The physical differences between these two $p$+Pb and Pb+Pb collision environments are further validated by Pearson linear correlation analyses. The correlation between the average transverse flow velocity ($< \beta_T >$) and the power-index $n$ is significantly positive in $p$+Pb collisions, but strongly negative ($R(<\beta_T>, n) \approx -1$) in Pb+Pb collisions. This is due to nearly opposite trends observed in $\langle N_{part} \rangle$ dependencies of power-index $n$ in $p$+Pb and Pb+Pb collisions: parameter $n$ on the whole increases with $\langle N_{part} \rangle$ in $p$+Pb collisions, whereas $n$ generally decreases with an increase in $\langle N_{part} \rangle$ in Pb+Pb collisions. Similarly, the correlation between non-extensivity parameter $q$ and freeze-out temperature, $T_0$, is practically absent in $p$+Pb, but strongly positive ($R(q, T_0) \approx +0.9$) in Pb+Pb collisions. This is due to significant differences in the $\langle N_{part} \rangle$ dependencies of $T_0$ in $p$+Pb and Pb+Pb systems. Similarly, the remaining differences in parameter correlations between the $p$+Pb and Pb+Pb systems in Tables 4 and 5 can be explained simply by distinct centrality ($\langle N_{part} \rangle$) dependencies of parameters $T_0$ and $n$ in $p$+Pb and Pb+Pb collisions.

Although both the small asymmetric ($p$+Pb) and large symmetric (Pb+Pb) collision systems show signs of partial thermalization and collective radial expansion in more central collisions, they appear to evolve through different dynamics. While high-energy heavy-ion (Pb+Pb) collisions are characterized by strong fluid-like expansion and cooling, the smaller $p$+Pb systems seem to be more influenced by localized partonic interactions and rapid decoupling. These results establish critical benchmarks for theoretical models describing the transition from microscopic interactions to collective behavior in high-energy collisions.

**Author Contributions:** Conceptualization and ideas of research, K.K.O. and F.-H.L.; methodology, K.K.O., A.F. and F.-H.L.; software, K.K.O., K.A.M., S.A.K. and A.T.; validation, K.K.O., F.-H.L. and I.A.L.; preparation of figures and tables, K.K.O., K.A.M., S.I. and E.B.; formal analysis, K.K.O., K.A.M., S.A.K. and A.T.; investigation, K.K.O., A.F., F.-H.L., I.A.L., K.A.M., S.A.K., A.T., S.I. and E.B.; writing—original draft, K.K.O. and F.-H.L.; review and editing original draft, K.K.O., A.F., I.A.L. and F.-H.L. All authors have read and agreed to the published version of the manuscript.

**Funding:** The research work was supported by the Science Committee of the Ministry of Education and Science of the Republic of Kazakhstan (Grant No. AP23487706). The work of PTI authors (Uzbekistan) was supported by the State Budget of Uzbekistan through the Uzbekistan Academy of Sciences. The work of F.-H.L. was supported by the National Natural Science Foundation of China (Grant No. 12147215) and the Shanxi Provincial Basic Research Program (Natural Science Foundation) under Grant No. 202303021212293.

**Data Availability Statement:** The data analyzed in this article are included within the paper and cited as references at relevant places within the text of the manuscript.

**Conflicts of Interest:** The authors do not have any conflicts of interest regarding the article.

## References

1. Acharya, S. et al. [ALICE Collaboration] The ALICE experiment: A journey through QCD. *Eur. Phys. J. C* **2024**, *84*, 813. [CrossRef]
2. Arsene, I. et al. [BRAHMS Collaboration] Quark–gluon plasma and color glass condensate at RHIC? The perspective from the BRAHMS experiment. *Nucl. Phys. A* **2005**, *757*, 1–27. [CrossRef]
3. Adcox, K. et al. [PHENIX Collaboration] Formation of dense partonic matter in relativistic nucleus–nucleus collisions at RHIC: Experimental evaluation by the PHENIX Collaboration. *Nucl. Phys. A* **2005**, *757*, 184. [CrossRef]

4. Back, B.B. et al. [PHOBOS Collaboration] The PHOBOS perspective on discoveries at RHIC. *Nucl. Phys. A* **2005**, *757*, 28–101. [CrossRef]
5. Adams, J. et al. [STAR Collaboration] Experimental and theoretical challenges in the search for the quark–gluon plasma: The STAR Collaboration's critical assessment of the evidence from RHIC collisions. *Nucl. Phys. A* **2005**, *757*, 102. [CrossRef]
6. Shuryak, E. What RHIC experiments and theory tell us about properties of quark–gluon plasma? *Nucl. Phys. A* **2005**, *750*, 64. [CrossRef]
7. Chatrchyan, S. et al. [CMS Collaboration] Observation and studies of jet quenching in PbPb collisions at $\sqrt{s_{nn}}$ = 2.76 TeV. *Phys. Rev. C* **2011**, *84*, 024906. [CrossRef]
8. Song, H.; Bass, S.A.; Heinz, U.; Hirano, T.; Shen, C. 200 A GeV Au+Au Collisions Serve a Nearly Perfect Quark-Gluon Liquid. *Phys. Rev. Lett.* **2011**, *106*, 192301. [CrossRef] [PubMed]
9. Heinz, U.; Snellings, R. Collective Flow and Viscosity in Relativistic Heavy-Ion Collisions. *Ann. Rev. Part. Sci.* **2013**, *63*, 123. [CrossRef]
10. Adamczyk, L. et al. [STAR Collaboration] Bulk Properties of the Medium Produced in Relativistic Heavy-Ion Collisions from the Beam Energy Scan Program. *Phys. Rev. C* **2017**, *96*, 044904. [CrossRef]
11. Braun-Munzinger, P.; Redlich, K.; Stachel, J. Particle production in heavy ion collisions. In *Quark Gluon Plasma 3*; Hwa, R.C., Wang, X.-N., Eds.; World Scientific Publishing: Singapore, 2004.
12. Andronic, A.; Braun-Munzinger, P.; Stachel, J. Hadron production in central nucleus-nucleus collisions at chemical freezeout. *Nucl. Phys. A* **2006**, *772*, 167. [CrossRef]
13. Becattini, F.; Manninen, J.; Gazdzicki, M. Energy and system size dependence of chemical freeze-out in relativistic nuclear collisions. *Phys. Rev. C* **2006**, *73*, 044905. [CrossRef]
14. Andronic, A.; Braun-Munzinger, P.; Stachel, J. Thermal hadron production in relativistic nuclear collisions: The Hadron mass spectrum, the horn, and the QCD phase transition. *Phys. Lett. B* **2009**, *673*, 142. [CrossRef]
15. Stachel, J.; Andronic, A.; Braun-Munzinger, P.; Redlich, K. Confronting LHC data with the statistical hadronization model. *J. Phys. Conf. Ser.* **2014**, *509*, 012019. [CrossRef]
16. Adam, J. et al. [ALICE Collaboration] Enhanced production of multi-strange hadrons in high-multiplicity proton–proton collisions. *Nat. Phys.* **2017**, *13*, 535. [CrossRef]
17. Tripathy, S. et al. [ALICE Collaboration] Energy dependence of φ(1020) production at mid-rapidity in *pp* collisions with ALICE at the LHC. *Nucl. Phys. A* **2019**, *982*, 180. [CrossRef]
18. Dash, A.K. et al. [ALICE Collaboration] Multiplicity dependence of strangeness and hadronic resonance production in *pp* and *p*-Pb collisions with ALICE at the LHC. *Nucl. Phys. A* **2019**, *982*, 467. [CrossRef]
19. Acharya, S. et al. [ALICE Collaboration] Multiplicity dependence of light flavor hadron production in *pp* collisions at $(s_{nn})^{1/2}$ = 7 TeV. *Phys. Rev. C* **2019**, *99*, 024906.
20. Khuntia, A.; Sharma, H.; Tiwari, S.K.; Sahoo, R.; Cleymans, J. Radial flow and differential freeze-out in proton-proton collisions at $(s)^{1/2}$ = 7 TeV at the LHC. *Eur. Phys. J. A* **2019**, *55*, 3. [CrossRef]
21. Csanád, M.; Csörgő, T.; Jiang, Z.-F.; Yang, C.-B. Initial energy density of $(s_{nn})^{1/2}$ = 7 and 8 TeV *p-p* collisions at LHC. *Universe* **2017**, *3*, 9. [CrossRef]
22. Baptista, R.P.; Rocha, L.Q.; Menezes, D.P.; Trevisan, L.A.; Tsallis, C.; Deppman, A. Evidence of fractal structures in hadrons. *Eur. Phys. J. A* **2024**, *60*, 93. [CrossRef]
23. Tripathy, S.; Bisht, A.; Sahoo, R.; Khuntia, A.; Salvan, M.P. Event shape and multiplicity dependence of freeze-out scenario and system thermodynamics in proton+proton collisions at $(s_{nn})^{1/2}$ = 13 TeV using PYTHIA8. *Adv. High Energy Phys.* **2021**, *2021*, 8822524.
24. Jiang, K.; Zhu, Y.; Liu, W.; Chen, H.; Li, C.; Ruan, L.; Tang, Z.; Xu, Z. Onset of radial flow in *p+p* collisions. *Phys. Rev. C* **2015**, *91*, 024910. [CrossRef]
25. Bashir, I.-U.; Bhat, R.A.; Uddin, S. Evidence of collective flow in *p-p* collisions at LHC. *arXiv* **2015**, arXiv:1502.04185v2.
26. Bashir, I.-U.; Parra, R.A.; Bhat, R.A.; Uddin, S. Particle Transverse Momentum Distributions in *p-p* Collisions at $(s)^{1/2}$ = 0.9 TeV. *Adv. High Energy Phys.* **2019**, *2019*, 8219567. [CrossRef]
27. Baker, O.K.; Kharzeev, D.E. Thermal radiation and entanglement in proton-proton collisions at energies available at the CERN Large Hadron Collider. *Phys. Rev. D* **2018**, *98*, 054007. [CrossRef]
28. Kharzeev, D.E.; Levin, E.M. Deep inelastic scattering as a probe of entanglement. *Phys. Rev. D* **2017**, *95*, 114008. [CrossRef]
29. Bergers, J.; Floerchinger, S.; Venugopalan, R. Dynamics of entanglement in expanding quantum fields. *J. High Energy Phys.* **2018**, *4*, 145. [CrossRef]
30. Bergers, J.; Floerchinger, S.; Venugopalan, R. Thermal excitation spectrum from entanglement in an expanding quantum string. *Phys. Lett. B* **2018**, *778*, 442. [CrossRef]
31. Feal, X.; Pajares, C.; Vazquez, R.A. Thermal behavior and entanglement in Pb-Pb and p−p collisions. *Phys. Rev. C* **2019**, *99*, 015205. [CrossRef]

32. Gu, J.; Li, C.; Wang, Q.; Zhang, W.; Zheng, H. Collective expansion in pp collisions using the Tsallis statistics. *J. Phys. G* **2022**, *49*, 115101. [CrossRef]
33. Olimov, K.K.; Liu, F.-H.; Musaev, K.; Shodmonov, M. Multiplicity Dependencies of Midrapidity Transverse Momentum Distributions of Identified Charged Particles in Proton-Proton Collisions at $(s)^{1/2}$ = 7 TeV at the LHC. *Universe* **2022**, *8*, 174. [CrossRef]
34. Olimov, K.K.; Liu, F.-H.; Musaev, K.A.; Tukhtaev, B.J.; Yuldashev, B.S.; Saidkhanov, N.S.; Umarov, K.I.; Gulamov, K.G. Multiplicity dependencies of midrapidity transverse momentum spectra of identified charged particles in *p*+*p* collisions at $(s)^{1/2}$ = 13 TeV at LHC. *Int. J. Mod. Phys. A* **2021**, *36*, 2150149. [CrossRef]
35. Olimov, K.K.; Lebedev, I.A.; Fedosimova, A.I.; Liu, F.-H.; Dmitriyeva, E.; Musaev, K.A.; Olimov, K.; Yuldashev, B.S. Correlations among parameters of the Tsallis distribution and Hagedorn function with embedded transverse flow in proton–proton collisions at $(s)^{1/2}$ = 7 and 13 TeV. *Eur. Phys. J. Plus* **2023**, *138*, 414. [CrossRef]
36. Waqas, M.; Liu, F.-H.; Ben Slimane, J.; Olimov, K.; Ajaz, M.; Alrebdi, H.; Ismail, A.H. Multiplicity dependent behavior of thermodynamic parameters in proton–proton collisions at 13 TeV. *Ann. Phys.* **2025**, *481*, 170180. [CrossRef]
37. Badshah, M.; Waqas, M.; Khubrani, A.M.; Ajaz, M. Systematic analysis of the pp collisions at LHC energies with Tsallis function. *Europhys. Lett.* **2023**, *141*, 64002. [CrossRef]
38. Li, L.-L.; Waqas, M.; Ajaz, M.; Khubrani, A.M.; Yao, H.; Khan, M.A. Analyses of pp, Cu–Cu, Au–Au and Pb–Pb Collisions by Tsallis-Pareto Type Function at RHIC and LHC Energies. *Entropy* **2022**, *24*, 1219. [CrossRef] [PubMed]
39. Chatrchyan, S. et al. [CMS Collaboration] Study of the production of charged pions, kaons, and protons in p-Pb collisions at $\sqrt{s_{nn}}$ = 5.02 TeV. *Eur. Phys. J. C* **2014**, *74*, 2847. [PubMed]
40. Chatrchyan, S. et al. [CMS Collaboration] Observation of long-range near-side angular correlations in proton-lead collisions at the LHC. *Phys. Lett. B* **2013**, *718*, 795–814.
41. Abelev, B. et al. [ALICE Collaboration] Long-range angular correlations on the near and away side in p-Pb collisions at $\sqrt{s_{nn}}$ = 5.02 TeV. *Phys. Lett. B* **2013**, *719*, 29–41. [CrossRef]
42. Aad, G. et al. [ATLAS Collaboration] Observation of associated near-side and away-side long-range correlations in $\sqrt{s_{nn}}$ = 5.02 TeV proton-lead collisions with the ATLAS detector. *Phys. Rev. Lett.* **2013**, *110*, 182302. [CrossRef] [PubMed]
43. Adam, J. et al. [ALICE Collaboration] Multiplicity dependence of charged pion, kaon, and (anti)proton production at large transverse momentum in p–Pb collisions at $\sqrt{s_{nn}}$ = 5.02 TeV. *Phys. Lett. B* **2016**, *760*, 720. [CrossRef]
44. Abelev, B.B. et al. [ALICE Collaboration] Multiplicity dependence of pion, kaon, proton and lambda production in p-Pb Collisions at $\sqrt{s_{nn}}$ = 5.02 TeV. *Phys. Lett. B* **2014**, *728*, 25. [CrossRef]
45. Olimov, K.K.; Lebedev, I.A.; Fedosimova, A.I.; Liu, F.-H.; Sanetullaev, A.; Tokhirov, A.; Khudoyberdieva, S.A.; Yuldashev, B.S.; Kakhorova, A.N. Combined analysis of midrapidity transverse momentum distributions of the charged pions and kaons, protons and antiprotons in p+Pb collisions at $(s_{nn})^{1/2}$ = 5.02 TeV at the LHC. *Eur. Phys. J. Plus* **2024**, *139*, 457. [CrossRef]
46. Olimov, K.K.; Liu, F.-H.; Musaev, K.A.; Olimov, K.; Shodmonov, M.Z.; Fedosimova, A.I.; Lebedev, I.A.; Kanokova, S.Z.; Tukhtaev, B.J.; Yuldashev, B.S. Study of midrapidity $p_T$ distributions of identified charged particles in Xe+Xe collisions at $(s_{nn})^{1/2}$ = 5.44 TeV using non-extensive Tsallis statistics with transverse flow. *Mod. Phys. Lett. A* **2022**, *37*, 2250095. [CrossRef]
47. Olimov, K.K.; Liu, F.-H.; Fedosimova, A.I.; Lebedev, I.A.; Deppman, A.; Musaev, K.A.; Shodmonov, M.Z.; Tukhtaev, B.J. Analysis of Midrapidity $p_T$ Distributions of Identified Charged Particles in Pb + Pb Collisions at $(s_{nn})^{1/2}$ = 5.02 TeV Using Tsallis Distribution with Embedded Transverse Flow. *Universe* **2022**, *8*, 401. [CrossRef]
48. Olimov, K.K.; Lebedev, I.A.; Fedosimova, A.I.; Liu, F.-H.; Kanokova, S.Z.; Shodmonov, M.Z.; Tukhtaev, B.J. Simultaneous Analysis of Midrapidity $p_T$ Spectra of Identified Particle Species in Pb + Pb Collisions at $(s_{nn})^{1/2}$ = 2.76 TeV Using Tsallis Distribution with Transverse Flow. *Universe* **2022**, *8*, 655. [CrossRef]
49. Bediaga, I.; Curado, E.M.F.; de Miranda, J.M. A nonextensive thermodynamical equilibrium approach in e+e− → hadrons. *Phys. A Stat. Mech. Its Appl.* **2000**, *286*, 156–163. [CrossRef]
50. Olimov, K.K.; Gulamov, K.G.; Liu, F.-H.; Olimov, K.; Khudoyberdieva, S.A.; Musaev, K.A.; Kanokova, S.Z. Description of midrapidity $p_T$ spectra of primary charged particles with changing centrality and energy of Pb+Pb and Xe+Xe collisions at the LHC with a two-component model. *Preprints* **2026**, 2026071892. [CrossRef]
51. Acharya, S. et al. [ALICE Collaboration] Transverse momentum spectra and nuclear modification factors of charged particles in pp, p-Pb and Pb-Pb collisions at the LHC. *J. High Energy Phys.* **2018**, *2018*, 13. [CrossRef]
52. Acharya, S. et al. [ALICE Collaboration] Transverse momentum spectra and nuclear modification factors of charged particles in Xe-Xe collisions at $\sqrt{s_{nn}}$ = 5.44 TeV. *Phys. Lett. B* **2019**, *788*, 166–179. [CrossRef]
53. Acharya, S. et al. [ALICE Collaboration] Centrality Determination in Heavy Ion Collisions. CERN Preprint ALICE-PUBLIC-2018-011. Available online: https://cds.cern.ch/record/2636623/files/centrality%20determination%20note.pdf (accessed on 1 May 2026).
54. Adam, J. et al. [ALICE Collaboration] Centrality dependence of particle production in p-Pb collisions at $\sqrt{s_{nn}}$ = 5.02 TeV. *Phys. Rev. C* **2015**, *91*, 064905. [CrossRef]

55. Cleymans, J.; Lykasov, G.I.; Parvan, A.S.; Sorin, A.S.; Teryaev, O.V.; Worku, D. Systematic properties of the Tsallis Distribution: Energy Dependence of Parameters in High-Energy *p-p* Collisions. *Phys. Lett. B* **2013**, *723*, 351. [CrossRef]
56. Cleymans, J.; Worku, D. The Tsallis distribution in proton–proton collisions at $(s_{\mathrm{nn}})^{1/2}$ = 0.9 TeV at the LHC. *J. Phys. G* **2012**, *39*, 025006. [CrossRef]
57. Zheng, H.; Zhu, L. Comparing the Tsallis Distribution with and without Thermodynamical Description in *p-p* Collisions. *Adv. High Energy Phys.* **2016**, *2016*, 9632126. [CrossRef]
58. Tsallis, C. Possible generalization of Boltzmann-Gibbs statistics. *J. Stat. Phys.* **1988**, *52*, 479. [CrossRef]
59. Tsallis, C. Nonadditive entropy: The concept and its use. *Eur. Phys. J. A* **2009**, *40*, 257. [CrossRef]
60. Tsallis, C.; Mendes, R.; Plastino, A.R. The role of constraints within generalized nonextensive statistics. *Physica A* **1998**, *261*, 534. [CrossRef]
61. Khandai, P.K.; Sett, P.; Shukla, P.; Singh, V. Hadron spectra in *p+p* collisions at RHIC and LHC energies. *Int. J. Mod. Phys. A* **2013**, *28*, 1350066. [CrossRef]
62. Hagedorn, R. Multiplicities, $p_{\mathrm{T}}$ Distributions and the Expected Hadron $\rightarrow$ Quark-Gluon Phase Transition. *Riv. Nuovo Cim.* **1983**, *6*, 1–50. [CrossRef]
63. Saraswat, K.; Shukla, P.; Singh, V. Transverse momentum spectra of hadrons in high energy pp and heavy ion collisions. *J. Phys. Commun.* **2018**, *2*, 035003. [CrossRef]
64. Brodsky, S.J.; Pirner, H.J.; Raufeisen, J. Scaling properties of high $p_T$ inclusive hadron production. *Phys. Lett. B* **2006**, *637*, 58–63. [CrossRef]
65. Abelev, B. et al. [ALICE Collaboration] Centrality dependence of $\pi$, *K*, and *p* production in Pb-Pb collisions at $(s_{\mathrm{nn}})^{1/2}$ = 2.76 TeV. *Phys. Rev. C* **2013**, *88*, 044910. [CrossRef]
66. Acharya, S. et al. [ALICE Collaboration] Production of charged pions, kaons and (anti-)protons in Pb-Pb and inelastic pp collisions at $\sqrt{s_{nn}}$ = 5.02 TeV. *Phys. Rev. C* **2020**, *101*, 044907. [CrossRef]
67. Olimov, K.K.; Lebedev, I.A.; Fedosimova, A.I.; Liu, F.-H.; Tokhirov, A.; Khudoyberdieva, S.A.; Kurbanov, A.R. Centrality evolution of transverse momentum spectra of primary charged particles produced in high-energy Pb+Pb collisions at the LHC. *Mod. Phys. Lett. A* **2026**, *41*, 2650120. [CrossRef]


**Disclaimer/Publisher's Note:** The statements, opinions and data contained in all publications are solely those of the individual author(s) and contributor(s) and not of MDPI and/or the editor(s). MDPI and/or the editor(s) disclaim responsibility for any injury to people or property resulting from any ideas, methods, instructions or products referred to in the content.